

Revisiting Sliced Wasserstein on Images: From Vectorization to Convolution

Khai Nguyen[†] Nhat Ho[†]

University of Texas, Austin[†]

April 4, 2022

Abstract

The conventional sliced Wasserstein is defined between two probability measures that have realizations as *vectors*. When comparing two probability measures over images, practitioners first need to vectorize images and then project them to one-dimensional space by using matrix multiplication between the sample matrix and the projection matrix. After that, the sliced Wasserstein is evaluated by averaging the two corresponding one-dimensional projected probability measures. However, this approach has two limitations. The first limitation is that the spatial structure of images is not captured efficiently by the vectorization step; therefore, the later slicing process becomes harder to gather the discrepancy information. The second limitation is memory inefficiency since each slicing direction is a vector that has the same dimension as the images. To address these limitations, we propose novel slicing methods for sliced Wasserstein between probability measures over images that are based on the convolution operators. We derive *convolution sliced Wasserstein* (CSW) and its variants via incorporating stride, dilation, and non-linear activation function into the convolution operators. We investigate the metricity of CSW as well as its sample complexity, its computational complexity, and its connection to conventional sliced Wasserstein distances. Finally, we demonstrate the favorable performance of CSW over the conventional sliced Wasserstein in comparing probability measures over images and in training deep generative modeling on images¹.

1 Introduction

Optimal transport and Wasserstein distance [53, 46] have become popular tools in machine learning and data science. For example, optimal transport has been utilized in generative modeling tasks to generate realistic images [2, 52], in domain adaptation applications to transfer knowledge from source to target domains [9, 3], in clustering applications to capture the heterogeneity of data [20], and in other applications [28, 56, 57]. Despite having appealing performance, Wasserstein distance has been known to suffer from high computational complexity, namely, its computational complexity is at the order of $\mathcal{O}(m^3 \log m)$ [44] when the probability measures have at most m supports. In addition, Wasserstein distance also suffers from the curse of dimensionality, namely, its sample complexity is at the order of $\mathcal{O}(n^{-1/d})$ [14] where n is the sample size. A popular line of works to improve the speed of computation and the sample complexity of the Wasserstein distance is by adding an entropic regularization term to the Wasserstein distance [10]. This variant is known as entropic regularized optimal transport (or equivalently entropic regularized Wasserstein). By using the entropic version, we can approximate the value of Wasserstein distance with the computational complexities being at the order of $\mathcal{O}(n^2)$ [1, 34, 35, 33] (up to some polynomial orders of approximation errors).

¹Code for the paper will be published at <https://github.com/UT-Austin-Data-Science-Group/CSW>.

Furthermore, the sample complexity of the entropic version had also been shown to be at the order of $\mathcal{O}(n^{-1/2})$ [38], which indicates that it does not suffer from the curse of dimensionality.

Another useful line of works to improve both the computational and sample complexities of the Wasserstein distance is based on the closed-form solution of optimal transport in one dimension. A notable distance along this direction is sliced Wasserstein (SW) distance [6]. Due to the fast computational complexity $\mathcal{O}(m \log_2 m)$ and no curse of dimensionality $\mathcal{O}(n^{-1/2})$, the sliced Wasserstein has been applied successfully in several applications, such as generative modeling [55, 13, 24], domain adaptation [30], and clustering [25]. The sliced Wasserstein is defined between two probability measures that have supports belonging to a vector space, e.g, \mathbb{R}^d . As defined in [6], the sliced Wasserstein is written as the expectation of one-dimensional Wasserstein distance between two projected measures over the uniform distribution on the unit sphere. Due to the intractability of the expectation, Monte Carlo samples from the uniform distribution over the unit sphere are used to approximate the sliced Wasserstein distance. The number of samples is often called the number of projections and it is denoted as L . On the computational side, the computation of sliced Wasserstein can be decomposed into two steps. In the first step, L projecting directions are first sampled and then are stacked as a matrix (the projection matrix). After that, the projection matrix is multiplied by the two data matrices resulting in two matrices that represent L one-dimensional projected probability measures. In the second step, L one-dimensional Wasserstein distances are computed between the two corresponding projected measures with the same projecting direction. Finally, the average of those distances is yielded as the value of the sliced Wasserstein.

Despite being applied widely in tasks that deal with probability measures over images [55, 13], the conventional formulation of sliced Wasserstein is not well-defined to the nature of images. In particular, an image is not a vector but is a tensor. Therefore, a probability measure over images should be defined over the space of tensors instead of images. The conventional formulation leads to an extra step in using the sliced Wasserstein on the domain of images which is vectorization. Namely, all images (supports of two probability measures) are transformed into vectors by a deterministic one-one mapping which is the "reshape" operator. This extra step does not keep the spatial structures of the supports, which are crucial information of images. Furthermore, the vectorization step also poses certain challenges to design efficient ways of projecting (slicing) samples to one dimension based on prior knowledge about the domain of samples. Finally, prior empirical investigations indicate that there are several slices in the conventional Wasserstein collapsing the two probability measures to the Dirac Delta at zero [13, 12, 23]. Therefore, these slices do not contribute to the overall discrepancy. These works suggest that the space of projecting directions in the conventional sliced Wasserstein (the unit hyper-sphere) is potentially not optimal, at least for images.

Contribution. To address these issues of the sliced Wasserstein over images, we propose to replace the conventional formulation of the sliced Wasserstein with a new formulation that is defined on the space of probability measures over tensors. Moreover, we also propose a novel slicing process by changing the conventional matrix multiplication to the convolution operators [15, 17]. In summary, our main contributions are two-fold:

1. We leverage the benefits of the convolution operators on images, including their efficient parameter sharing and memory saving as well as their superior performance in several tasks on images [27, 18], to introduce efficient slicing methods on sliced Wasserstein, named *convolution slicers*. With the convolution slicers, we derive a novel variant of sliced Wasserstein, named *convolution sliced Wasserstein* (CSW). We investigate the metricity of CSW, its sample and

computational complexities, and its connection to other variants of sliced Wasserstein.

2. We then illustrate the favorable performance of CSW in comparing probability measures over images. In particular, we show that CSW provides an almost identical discrepancy between MNIST’s digits compared to that of the SW while having much less slicing memory. Furthermore, we compare SW and CSW in training deep generative models on standard benchmark images datasets, including CIFAR10, CelebA, STL10, and CeleA-HQ. By considering quality of the trained generative models, training speed, and training memory of CSW and SW, we observe that the CSW has more favorable performance than the vanilla SW.

Organization. The remainder of the paper is organized as follows. We first provide background about Wasserstein distance, the conventional slicing process in the sliced Wasserstein distance, and the convolution operator in Section 2. In Section 3, we propose the convolution slicing and the convolution sliced Wasserstein, and analyze some of its theoretical properties. The discussion on related works is given in Section 4. Section 5 contains the application of CSW to generative models, qualitative experimental results, and quantitative experimental results on standard benchmarks. We conclude the paper in Section 6. Finally, we defer the proofs of key results and extra materials in the Appendices.

Notation. For any $d \geq 2$, $\mathbb{S}^{d-1} := \{\theta \in \mathbb{R}^d \mid \|\theta\|_2^2 = 1\}$ denotes the d dimensional unit hyper-sphere in \mathcal{L}_2 norm, and $\mathcal{U}(\mathbb{S}^{d-1})$ is the uniform measure over \mathbb{S}^{d-1} . Moreover, δ denotes the Dirac delta function. For $p \geq 1$, $\mathcal{P}_p(\mathbb{R}^d)$ is the set of all probability measures on \mathbb{R}^d that have finite p -moments. For $\mu, \nu \in \mathcal{P}_p(\mathbb{R}^d)$, $\Pi(\mu, \nu) := \{\pi \in \mathcal{P}_p(\mathbb{R}^d \times \mathbb{R}^d) \mid \int_{\mathbb{R}^d} \pi(x, y) dx = \nu, \int_{\mathbb{R}^d} \pi(x, y) dy = \mu\}$ is the set of transportation plans between μ and ν . For $m \geq 1$, we denote $\mu^{\otimes m}$ as the product measure which has the support is m random variables follows μ . For a vector $X \in \mathbb{R}^{dm}$, $X := (x_1, \dots, x_m)$, P_X denotes the empirical measures $\frac{1}{m} \sum_{i=1}^m \delta_{x_i}$. For any two sequences a_n and b_n , the notation $a_n = \mathcal{O}(b_n)$ means that $a_n \leq C b_n$ for all $n \geq 1$ where C is some universal constant.

2 Background

In this section, we first review the definitions of the Wasserstein distance, the conventional slicing, and the sliced Wasserstein distance, and discuss its limitation. We then review the convolution and the padding operators on images.

Sliced Wasserstein: For any $p \geq 1$ and dimension $d' \geq 1$, we first define the Wasserstein- p distance [53, 45] between two probability measures $\mu \in \mathcal{P}_p(\mathbb{R}^{d'})$ and $\nu \in \mathcal{P}_p(\mathbb{R}^{d'})$, which is given by:

$$W_p(\mu, \nu) := \left(\inf_{\pi \in \Pi(\mu, \nu)} \int_{\mathbb{R}^{d'} \times \mathbb{R}^{d'}} \|x - y\|_p^p d\pi(x, y) \right)^{\frac{1}{p}}. \quad (1)$$

When $d' = 1$, the Wasserstein distance has a closed form which is $W_p(\mu, \nu) = (\int_0^1 |F_\mu^{-1}(z) - F_\nu^{-1}(z)|^p dz)^{1/p}$ where F_μ and F_ν are the cumulative distribution function (CDF) of μ and ν respectively. Given this closed-form property of Wasserstein distance in one dimension, the sliced Wasserstein distance [6] between μ and ν had been introduced and admitted the following formulation:

$$SW_p(\mu, \nu) := \left(\int_{\mathbb{S}^{d-1}} W_p^p(\theta \# \mu, \theta \# \nu) d\theta \right)^{\frac{1}{p}}, \quad (2)$$

where $\theta_{\#}\mu$ is the push-forward probability measure of μ through the function $T_{\theta} : \mathbb{R}^{d'} \rightarrow \mathbb{R}$ with $T_{\theta}(x) = \theta^{\top}x$. For each $\theta \in \mathbb{S}^{d'-1}$, $W_p^p(\theta_{\#}\mu, \theta_{\#}\nu)$ can be computed in linear time $\mathcal{O}(m \log_2 m)$ where m is the number of supports of μ and ν . However, the integration over the unit sphere in the sliced Wasserstein distance is intractable to compute. Therefore, Monte Carlo scheme is employed to approximate the integration, namely, $\theta_1, \dots, \theta_L \sim \mathcal{U}(\mathbb{S}^{d'-1})$ are drawn uniformly from the unit sphere and the approximation of the sliced Wasserstein distance is given by:

$$\text{SW}_p(\mu, \nu) \approx \left(\frac{1}{L} \sum_{i=1}^L W_p^p(\theta_i \# \mu, \theta_i \# \nu) \right)^{\frac{1}{p}}. \quad (3)$$

In practice, the number of projections L should be chosen to be sufficiently large compared to the dimension d' . It can be undesirable since the computational complexity of SW is linear with L .

Sliced Wasserstein on Images: Now, we focus on two probability measures over images: $\mu, \nu \in \mathcal{P}_p(\mathbb{R}^{c \times d \times d})$ for number of channels $c \geq 1$ and dimension $d \geq 1$. In this case, the sliced Wasserstein between μ and ν is defined as:

$$\text{SW}_p(\mu, \nu) = \text{SW}_p(\mathcal{R}\#\mu, \mathcal{R}\#\nu), \quad (4)$$

where $\mathcal{R} : \mathbb{R}^{c \times d \times d} \rightarrow \mathbb{R}^{cd^2}$ is a deterministic one-to-one "reshape" mapping.

The slicing process: The slicing of sliced Wasserstein distance on probability measures over images consists of two steps: vectorization and projection. For better understanding, we visualize an example of projecting a probability measure $\mu \in \mathbb{R}^{c \times d \times d}$ that has n supports in Figure 1. In short, supports of μ are transformed into vectors in \mathbb{R}^{cd^2} and are stacked as a matrix of size $n \times cd^2$. A projection matrix of size $L \times cd^2$ is then sampled and has each column as a random vector following the uniform measure over the unit hyper-sphere. Finally, the multiplication of those two matrices returns L projected probability measures of n supports in one dimension.

Limitation of the conventional slicing: First of all, images contain spatial relations across channels and local information. Therefore, transforming images into vectors makes it challenging to obtain that information. Second, vectorization leads to the usage of projecting directions from the unit hyper-sphere, which can have several directions that do not have good discriminative power. Finally, sampling projecting directions in high-dimension is also time-consuming and memory-consuming. As a consequence, avoiding the vectorization step can improve the efficiency of the whole process.

Convolution operator: We now define the convolution operator on tensors [15], which will be used as an alternative way of projecting images to one dimension in the sliced Wasserstein. The definition of the convolution operator with stride and dilation is as follows.

Definition 1. (Convolution) Given the number of channels $c \geq 1$, the dimension $d \geq 1$, the stride size $s \geq 1$, the dilation size $b \geq 1$, the size of kernel $k \geq 1$, the convolution of a tensor $X \in \mathbb{R}^{c \times d \times d}$ with a kernel size $K \in \mathbb{R}^{c \times k \times k}$ is

$$X \overset{s,b}{*} K = Y, \quad Y \in \mathbb{R}^{1 \times d' \times d'},$$

where $d' = \frac{d-b(k-1)-1}{s} + 1$. For $i = 1, \dots, d'$ and $j = 1, \dots, d'$, $Y_{1,i,j}$ is defined as:

$$Y_{1,i,j} = \sum_{h=1}^c \sum_{i'=0}^{k-1} \sum_{j'=0}^{k-1} X_{h,s(i-1)+bi'+1,s(j-1)+bj'+1} \cdot K_{h,i'+1,j'+1}.$$

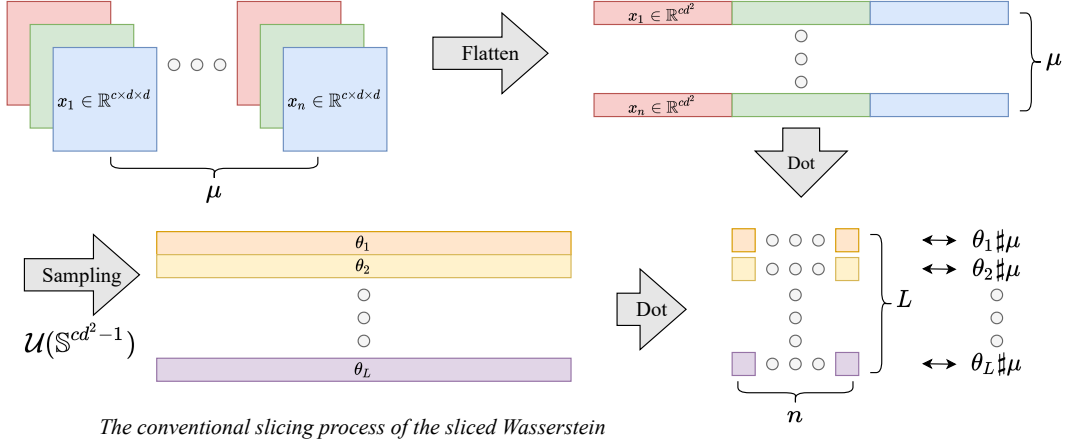


Figure 1: The conventional slicing process of sliced Wasserstein distance. The images $X_1, \dots, X_n \in \mathbb{R}^{c \times d \times d}$ are first flattened into vectors in \mathbb{R}^{cd^2} and then the Radon transform is applied to these vectors to lead to sliced Wasserstein (4) on images.

From its definition, we can check that the computational complexity of the convolution operator is $\mathcal{O}\left(c\left(\frac{d-b(k-1)-1}{s}+1\right)^2 k^2\right)$.

3 Convolution Sliced Wasserstein

In this section, we will define a convolution slicer that maps a tensor to a scalar by convolution operators. Moreover, we discuss the convolution slicer and some of its specific forms including the convolution-base slicer, the convolution-stride slicer, the convolution-dilation slicer, and their non-linear extensions. After that, we derive the convolution sliced Wasserstein (CSW), a family of variants of sliced Wasserstein, that utilizes a convolution slicer as the projecting method. Finally, we discuss some theoretical properties of CSW, namely, its metricity, its computational complexity, its sample complexity, and its connection to other variants of sliced Wasserstein.

3.1 Convolution Slicer

We first start with the definition of the convolution slicer, which plays an important role in defining convolution sliced Wasserstein.

Definition 2. (*Convolution Slicer*) For $N \geq 1$, given a sequence of kernels $K^{(1)} \in \mathbb{R}^{c^{(1)} \times d^{(1)} \times d^{(1)}}, \dots, K^{(N)} \in \mathbb{R}^{c^{(N)} \times d^{(N)} \times d^{(N)}}$, a convolution slicer $\mathcal{S}(\cdot | K^{(1)}, \dots, K^{(N)})$ on $\mathbb{R}^{c \times d \times d}$ is a composition of N convolution functions with kernels $K^{(1)}, \dots, K^{(N)}$ (with stride or dilation if needed) such that:

$$\mathcal{S}(X | K^{(1)}, \dots, K^{(N)}) \in \mathbb{R} \quad \forall X \in \mathbb{R}^{c \times d \times d}.$$

As indicated in Definition 2, the idea of the convolution slicer is to progressively map a given data X to a one-dimensional subspace through a sequence of convolution kernels, which capture spatial relations across channels as well as local information of the data. It is starkly different from the vectorization step in standard sliced Wasserstein on images (4).

Now, we will specify three particular types of convolution slicers based on using linear function on the convolution operator, named convolution-base, convolution-stride, and convolution-dilation slicers. We first start with the definition of the convolution-base slicer.

Definition 3. (*Convolution-base Slicer*) Given $X \in \mathbb{R}^{c \times d \times d}$ ($d \geq 2$),

1. When d is even, $N = \lceil \log_2 d \rceil$, sliced kernels are defined as $K^{(1)} \in \mathbb{R}^{c \times (2^{-1}d+1) \times (2^{-1}d+1)}$ and $K^{(h)} \in \mathbb{R}^{1 \times (2^{-h}d+1) \times (2^{-h}d+1)}$ for $h = 2, \dots, N-1$, and $K^{(N)} \in \mathbb{R}^{1 \times a \times a}$ where $a = \frac{d}{2^{N-1}}$. Then, the convolution-base slicer $\mathcal{CS}\text{-}b(X|K^{(1)}, \dots, K^{(N)})$ is defined as:

$$\mathcal{CS}\text{-}b(X|K^{(1)}, \dots, K^{(N)}) = X^{(N)}, \quad X^{(h)} = \begin{cases} X & h = 0 \\ X^{(h-1)} \underset{*}{\overset{1,1}{*}} K^{(h)} & 1 \leq h \leq N, \end{cases} \quad (5)$$

2. When d is odd, the convolution-base slicer $\mathcal{CS}\text{-}b(X|K^{(1)}, \dots, K^{(N)})$ takes the form:

$$\mathcal{CS}\text{-}b(X|K^{(1)}, \dots, K^{(N)}) = \mathcal{CS}\text{-}b(X \underset{*}{\overset{1,1}{*}} K^{(1)}|K^{(2)}, \dots, K^{(N)}), \quad (6)$$

where $K^{(1)} \in \mathbb{R}^{c \times 2 \times 2}$ and $K^{(2)}, \dots, K^{(N)}$ are the corresponding sliced kernels that are defined on the dimension $d-1$.

The idea of the convolution-base slicer in Definition 3 is to reduce the width and the height of the image by half after each convolution operator. If the width and the height of the image are odd, the first convolution operator is to reduce the size of the image by one via convolution with kernels of size 2×2 , and then the same procedure as that of the even case is applied. We would like to remark that the conventional slicing of sliced Wasserstein in Section 2 is equivalent to a convolution-base slicer $\mathcal{S}(\cdot|K^{(1)})$ where $K^{(1)} \in \mathbb{R}^{c \times d \times d}$ that satisfies the constraint $\sum_{h=1}^c \sum_{i=1}^d \sum_{j=1}^d K_{h,i,j}^{(1)2} = 1$.

We now discuss the second variant of the convolution slicer, named convolution-stride slicer, where we further incorporate stride into the convolution operators. Its definition is as follows.

Definition 4. (*Convolution-stride Slicer*) Given $X \in \mathbb{R}^{c \times d \times d}$ ($d \geq 2$),

1. When d is even, $N = \lceil \log_2 d \rceil$, sliced kernels are defined as $K^{(1)} \in \mathbb{R}^{c \times 2 \times 2}$ and $K^{(h)} \in \mathbb{R}^{1 \times 2 \times 2}$ for $h = 2, \dots, N-1$, and $K^{(N)} \in \mathbb{R}^{1 \times a \times a}$ where $a = \frac{d}{2^{N-1}}$. Then, the convolution-stride slicer $\mathcal{CS}\text{-}s(X|K^{(1)}, \dots, K^{(N)})$ is defined as:

$$\mathcal{CS}\text{-}s(X|K^{(1)}, \dots, K^{(N)}) = X^{(N)}, \quad X^{(h)} = \begin{cases} X & h = 0 \\ X^{(h-1)} \underset{*}{\overset{2,1}{*}} K^{(h)} & 1 \leq h \leq N-1, \\ X^{(h-1)} \underset{*}{\overset{1,1}{*}} K^{(h)} & h = N, \end{cases} \quad (7)$$

2. When d is odd, the convolution-stride slicer $\mathcal{CS}\text{-}s(X|K^{(1)}, \dots, K^{(N)})$ takes the form:

$$\mathcal{CS}\text{-}s(X|K^{(1)}, \dots, K^{(N)}) = \mathcal{CS}\text{-}s(X \underset{*}{\overset{1,1}{*}} K^{(1)}|K^{(2)}, \dots, K^{(N)}), \quad (8)$$

where $K^{(1)} \in \mathbb{R}^{c \times 2 \times 2}$ and $K^{(2)}, \dots, K^{(N)}$ are the corresponding sliced kernels that are defined on the dimension $d-1$.

Similar to the convolution-base slicer in Definition 3, the convolution-stride slicer reduces the width and the height of the image by half after each convolution operator. We use the same procedure of reducing the height and the width of the image by one when the height and the width of the image are odd. The benefit of the convolution-stride slicer is that the size of its kernels does not depend on the width and the height of images as that of the convolution-base slicer. This difference improves the computational complexity and time complexity of the convolution-stride slicer over those of the convolution-base slicer (cf. Proposition 1).

Now, we discuss the next variant of convolution slicer, named convolution-dilation slicer, where we include dilation with appropriate size into the convolution operators.

Definition 5. (*Convolution-dilation Slicer*) Given $X \in \mathbb{R}^{c \times d \times d}$ ($d \geq 2$),

1. When d is even, $N = \lceil \log_2 d \rceil$, sliced kernels are defined as $K^{(1)} \in \mathbb{R}^{c \times 2 \times 2}$ and $K^{(h)} \in \mathbb{R}^{1 \times 2 \times 2}$ for $h = 2, \dots, N - 1$, and $K^{(N)} \in \mathbb{R}^{1 \times a \times a}$ where $a = \frac{d}{2^{N-1}}$. Then, the convolution-dilation slicer $\mathcal{CS}\text{-}d(X|K^{(1)}, \dots, K^{(N)})$ is defined as:

$$\mathcal{CS}\text{-}d(X|K^{(1)}, \dots, K^{(N)}) = X^{(N)}, \quad X^{(h)} = \begin{cases} X & h = 0 \\ X^{(h-1)} \overset{1,2}{*} K^{(h)} & 1 \leq h \leq N - 1, \\ X^{(h-1)} \overset{1,1}{*} K^{(h)} & h = N, \end{cases} \quad (9)$$

2. When d is odd, the convolution-dilation slicer $\mathcal{CS}\text{-}d(X|K^{(1)}, \dots, K^{(N)})$ takes the form:

$$\mathcal{CS}\text{-}d(X|K^{(1)}, \dots, K^{(N)}) = \mathcal{CS}\text{-}d(X \overset{1,1}{*} K^{(1)}|K^{(2)}, \dots, K^{(N)}), \quad (10)$$

where $K^{(1)} \in \mathbb{R}^{c \times 2 \times 2}$ and $K^{(2)}, \dots, K^{(N)}$ are the corresponding sliced kernels that are defined on the dimension $d - 1$.

As with the previous slicers, the convolution-dilation slicer also reduces the width and the height of the image by half after each convolution operator and it uses the same procedure for the odd dimension cases. The design of kernels' size of the convolution-dilation slicer is the same as that of the convolution-stride slicer. However, the convolution-dilation slicer has a bigger receptive field in each convolution operator which might be appealing when the information of the image is presented by a big block of pixels.

Computational and projection memories complexities of the convolution slicers: We now establish the computational and projection memory complexities of convolution-base, convolution-stride, and convolution-dilation slicers in the following proposition. We would like to recall that the projection memory complexity is the memory that is needed to store a slice (convolution kernels).

Proposition 1. (a) When d is even, the computational and projection memory complexities of convolution-base slicer are respectively at the order of $\mathcal{O}(cd^4)$ and $\mathcal{O}(cd^2)$. When d is odd, these complexities are at the order of $\mathcal{O}(cd^2 + d^4)$ and $\mathcal{O}(c + d^2)$.

(b) The computational and projection memory complexities of convolution-stride slicer are respectively at the order of $\mathcal{O}(cd^2)$ and $\mathcal{O}(c + \lceil \log_2 d \rceil)$.

(c) The computational and projection memory complexities of convolution-dilation slicer are respectively at the order of $\mathcal{O}(cd^2)$ and $\mathcal{O}(c + \lceil \log_2 d \rceil)$.

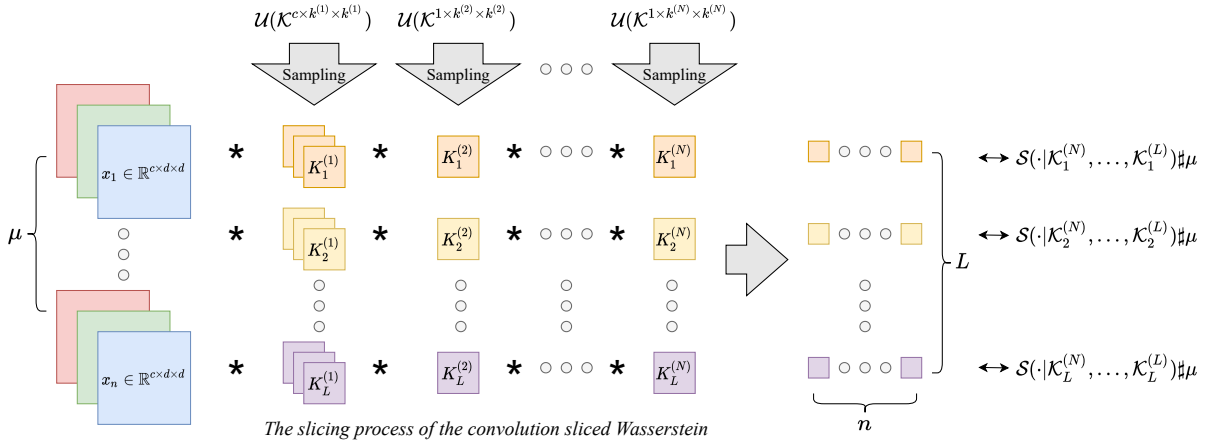


Figure 2: The convolution slicing process (using the convolution slicer). The images $X_1, \dots, X_n \in \mathbb{R}^{c \times d \times d}$ are directly mapped to a scalar by a sequence of convolution functions which have kernels as random tensors. This slicing process leads to the convolution sliced Wasserstein (11) on images.

Proof of Proposition 1 is in Appendix A.4. We recall that the computational complexity and the projection memory complexity of the conventional slicing in sliced Wasserstein are $\mathcal{O}(cd^2)$ and $\mathcal{O}(cd^2)$. We can observe that the convolution-base slicer has a worse computational complexity than the conventional slicing while having the same projection memory complexity. Since the size of kernels does not depend on the size of images, the convolution-stride slicer and the convolution-dilation slicer have the same computational complexity as the conventional slicing $\mathcal{O}(cd^2)$. However, their projection memory complexities are cheaper than conventional slicing, namely, $\mathcal{O}(c + \lceil \log_2 d \rceil)$ compared to $\mathcal{O}(cd^2)$.

Non-linear convolution-base slicer: The composition of convolution functions in the linear convolution slicer and its linear variants is still a linear function, which may not be effective when the data lie in a complex and highly non-linear low-dimensional subspace. A natural generalization of linear convolution slicers to enhance the ability of the slicers to capture the non-linearity of the data is to apply a non-linear activation function after convolution operators. This enables us to define a non-linear slicer in Definition 7 in Appendix B. The non-linear slicer can be seen as a defining function in generalized Radon Transform [47] which was used previously in generalized sliced Wasserstein [23].

3.2 Convolution Sliced Wasserstein

With the definition of convolution slicers on hand, we now state our general definition of convolution sliced Wasserstein. An illustration of the convolution sliced Wasserstein is given in Figure 2.

Definition 6. For any $p \geq 1$, the convolution sliced Wasserstein (CSW) of order $p > 0$ between two given probability measures $\mu, \nu \in \mathcal{P}_p(\mathbb{R}^{c \times d \times d})$ is given by:

$$CSW_p(\mu, \nu) := \left(\mathbb{E}_{K^{(1)} \sim \mathcal{U}(\mathcal{K}^{(1)}), \dots, K^{(N)} \sim \mathcal{U}(\mathcal{K}^{(N)})} \left[W_p^p \left(\mathcal{S}(\cdot | K^{(1)}, \dots, K^{(N)}) \# \mu, \mathcal{S}(\cdot | K^{(1)}, \dots, K^{(N)}) \# \nu \right) \right] \right)^{\frac{1}{p}}, \quad (11)$$

where $\mathcal{S}(\cdot|K^{(1)}, \dots, K^{(N)})$ is a convolution slicer with $K^{(i)} \in \mathbb{R}^{c^{(i)} \times k^{(i)} \times k^{(i)}}$ for any $i \in [N]$ and $\mathcal{U}(\mathcal{K}^{(i)})$ is the uniform distribution with the realizations being in the set $\mathcal{K}^{(i)}$ which is defined as $\mathcal{K}^{(i)} := \left\{ K^{(i)} \in \mathbb{R}^{c^{(i)} \times k^{(i)} \times k^{(i)}} \mid \sum_{h=1}^{c^{(i)}} \sum_{i'=1}^{k^{(i)}} \sum_{j'=1}^{k^{(i)}} K_{h,i',j'}^{(i)2} = 1 \right\}$, namely, the set $\mathcal{K}^{(i)}$ consists of tensors $K^{(i)}$ whose squared ℓ_2 norm is 1.

When we specifically consider the convolution slicer as convolution-base slicer (CS-b), convolution-stride slicer (CS-s), and convolution-dilation slicer (CS-d), we have the corresponding notions of convolution-base sliced Wasserstein (CSW-b), convolution-stride sliced Wasserstein (CSW-s), and convolution-dilation sliced Wasserstein (CSW-d).

Monte Carlo estimation and implementation: Similar to the conventional sliced Wasserstein, the expectation with respect to kernels $K^{(1)}, \dots, K^{(N)}$ uniformly drawn from the sets $\mathcal{K}^{(1)}, \dots, \mathcal{K}^{(N)}$ in the convolution sliced Wasserstein is intractable to compute. Therefore, we also make use of Monte Carlo method to approximate the expectation, which leads to the following approximation of the convolution sliced Wasserstein:

$$\text{CSW}_p(\mu, \nu) \approx \frac{1}{L} \sum_{i=1}^L W_p^p \left(\mathcal{S}(\cdot|K_i^{(1)}, \dots, K_i^{(N)}) \# \mu, \mathcal{S}(\cdot|K_i^{(1)}, \dots, K_i^{(N)}) \# \nu \right), \quad (12)$$

where $K_i^{(\ell)}$ are uniform samples from the sets $\mathcal{K}^{(\ell)}$ for any $\ell \in [N]$ and $i \in [L]$. Since each of the convolution slicer $\mathcal{S}(\cdot|K_i^{(1)}, \dots, K_i^{(N)})$ is in one dimension, we can utilize the closed-form expression of Wasserstein metric in one dimension to compute $W_p \left(\mathcal{S}(\cdot|K_i^{(1)}, \dots, K_i^{(N)}) \# \mu, \mathcal{S}(\cdot|K_i^{(1)}, \dots, K_i^{(N)}) \# \nu \right)$ with a complexity of $\mathcal{O}(m \log_2 m)$ for each $i \in [L]$ where m is the maximum number of supports of μ and ν . Therefore, the total computational complexity of computing the Monte Carlo approximation (12) is $\mathcal{O}(Lm \log_2 m)$ when the probability measures μ and ν have at most m supports. It is comparable to the computational complexity of sliced Wasserstein on images (4) where we directly vectorize the images and apply the Radon transform to these flatten images. Finally, for the implementation, we would like to remark that L convolution slicers in equation (12) can be computed *independently* and *parallelly* using the group convolution implementation which is supported in almost all libraries.

Properties of convolution sliced Wasserstein: We first have the following result for the metricity of the convolution sliced Wasserstein.

Theorem 1. *For any $p \geq 1$, the convolution sliced Wasserstein $\text{CSW}_p(\cdot, \cdot)$ is a pseudo-metric on the space of probability measures on $\mathbb{R}^{c \times d \times d}$, namely, it is symmetric, satisfies the triangle inequality, and $\text{CSW}_p(\mu, \nu) = 0 \iff \mu = \nu$.*

Proof of Theorem 1 is in Appendix A.1. Our next result establishes the connection between the convolution sliced Wasserstein and max-sliced Wasserstein and Wasserstein distances.

Proposition 2. *For any $p \geq 1$, we find that*

$$\text{CSW}_p(\mu, \nu) \leq \text{max-SW}_p(\mu, \nu) \leq W_p(\mu, \nu),$$

where $\text{max-SW}_p(\mu, \nu) := \max_{\theta \in \mathbb{R}^{cd^2}: \|\theta\| \leq 1} W_p(\theta \# \mu, \theta \# \nu)$ is max-sliced Wasserstein metric of order p between μ and ν .

Proof of Proposition 2 is in Appendix A.2. Given the bounds in Proposition 2, we demonstrate that the convolution sliced Wasserstein does not suffer from the curse of dimensionality for the inference purpose, namely, the sample complexity for the empirical distribution from i.i.d. samples to approximate their underlying distribution is at the order of $\mathcal{O}(n^{-1/2})$.

Proposition 3. *Assume that P is a probability measure supported on compact set of $\mathbb{R}^{c \times d \times d}$. Let X_1, X_2, \dots, X_n be i.i.d. samples from P and we denote $P_n = \frac{1}{n} \sum_{i=1}^n \delta_{X_i}$ as the empirical measure of these data. Then, for any $p \geq 1$, there exists a universal constant $C > 0$ such that*

$$\mathbb{E}[CSW_p(P_n, P)] \leq C \sqrt{\frac{(cd^2 + 1) \log n}{n}},$$

where the outer expectation is taken with respect to the data X_1, X_2, \dots, X_n .

Proof of Proposition 3 is in Appendix A.3. The result of Proposition 3 indicates that the sample complexity of the convolution sliced Wasserstein is comparable to that of the sliced Wasserstein on images (4), which is at the order of $\mathcal{O}(n^{-1/2})$ [4], and better than that of the Wasserstein metric, which is at the order of $\mathcal{O}(n^{-1/(2cd^2)})$ [14].

Extension to non-linear convolution sliced Wasserstein: In Appendix B, we provide a non-linear version of the convolution sliced Wasserstein, named non-linear convolution sliced Wasserstein. The high-level idea of the non-linear version is to incorporate non-linear activation functions to the convolution-base, convolution-stride, and convolution-dilation slicers. The inclusion of non-linear activation functions is to enhance the ability of slicers to capture the non-linearity of the data. By plugging these non-linear convolution slicers into the general definition of the convolution sliced Wasserstein in Definition 6, we obtain the non-linear variants of convolution sliced Wasserstein. Details of these variants are in Appendix B.

4 Related Works

Sliced Wasserstein is used for the pooling mechanism for aggregating a set of features in [39]. Sliced Wasserstein gradient flows are investigated in [37, 5]. Variational inference based on sliced Wasserstein is carried out in [58]. Similarly, sliced Wasserstein is used for approximate Bayesian computation in [40]. Statistical guarantees of training generative models with sliced Wasserstein is derived in [42]. Other frameworks for generative modeling using sliced Wasserstein are sliced iterative normalizing flows [11] and run-sort-rerun for fine-tuning pre-trained model [31]. Differentially private sliced Wasserstein is proposed in [48]. Approximating Wasserstein distance based on one-dimensional transportation plans from orthogonal projecting directions is introduced in [49]. To reduce the projection complexity of sliced Wasserstein, a biased approximation based on the concentration of Gaussian projections is proposed in [41]. Augmenting probability measures to a higher-dimensional space for a better linear separation is used in augmented sliced Wasserstein [7]. Projected Robust Wasserstein (PRW) metrics that find the best orthogonal linear projecting operator onto $k > 1$ dimensional space and Riemannian optimization techniques for solving it are proposed in [43, 32, 21]. Sliced Gromov Wasserstein, a fast sliced version of Gromov Wasserstein, is proposed in [51]. The slicing technique is also be applied in approximating mutual information [16]. We would like to recall that all the above works assume working with vector spaces and need to use vectorization when dealing with images.

5 Experiments

In this section, we focus on comparing the sliced Wasserstein (SW) (with the conventional slicing), the convolution-base sliced Wasserstein (CSW-b), the convolution sliced Wasserstein with stride (CSW-s), and the convolution sliced Wasserstein with dilation (CSW-d) on tasks that involve probability measures over images. In particular, we first show the values of the SW and the CSW variants between probability measures over digits of the MNIST dataset [29]. We then compare SW and several variants of CSW in training generative models on image datasets such as CIFAR10 (32x32) [26], STL10 (96x96) [8], CelebA (64x64), and CelebA-HQ (128x128) [36]. We recall that the number of projections in SW and CSW’s variants is denoted as L .

5.1 Comparing Measures over MNIST’s digits

In the MNIST dataset, there are 60000 images of size 28×28 of digits from 0 to 9. We compute SW between two empirical probability measures over images of every two digits, e.g., 1 and 2, 1 and 3, and so on. To compare on the same digit, e.g., 1, we split images of the same digit into two disjoint sets and then compute the SW between the corresponding empirical probability measures.

Meaningful measures of discrepancy: We approximate the SW and the CSW’s variants by a finite number of projections, namely, $L = 1$, $L = 10$, and $L = 100$. We show the mean of approximated values of $L = 100$ over 5 different runs and the corresponding standard deviation in Table 1. According to the table, we observe that SW and CSW’s variants can preserve discrepancy between digits well. In particular, the discrepancies between probability measures of the same digit are relatively small compared to the discrepancies between probability measures of different digits. Moreover, we see that the values of CSW-s and CSW-d are closed to the values of SW on the same pairs of digits. We also show similar tables for $L = 1$ and $L = 10$ in Tables 4-5 in Appendix C. From these tables, we observe that the number of projections can affect the stability of both SW and CSW’s variants.

Projection memory for slicers: For SW, the conventional slicing requires $L \cdot 784$ float variables for L projecting directions of $28 \cdot 28$ dimension. On the other hand, CSW only needs $L \cdot 338$ float variables since each projecting direction is represented as three kernels $K^{(1)} \in \mathbb{R}^{15 \times 15}$, $K^{(2)} \in \mathbb{R}^{8 \times 8}$, and $K^{(3)} \in \mathbb{R}^{7 \times 7}$. More importantly, CSW-s and CSW-d require only $L \cdot 57$ float variables since they are represented by three kernels $K^{(1)} \in \mathbb{R}^{2 \times 2}$, $K^{(2)} \in \mathbb{R}^{2 \times 2}$, and $K^{(3)} \in \mathbb{R}^{7 \times 7}$. From this experiment, we can see that using the whole unit-hypersphere as the space of projecting directions can be sub-optimal when dealing with images.

5.2 Generative Models

We follow the framework of sliced Wasserstein generator in [13]. In particular, we parameterize the model distribution $p_\phi(x) \in \mathcal{P}(\mathbb{R}^{c \times d \times d})$ and $p_\phi(x) = G_\phi \# \epsilon$ where ϵ is the standard multivariate Gaussian of 128 dimension and G_ϕ is a neural network with Resnet architecture [18]. Since the ground truth metric between images is unknown, we need a discriminator as a type of ground metric learning. We denote the discriminator as a function $T_{\beta_2} \circ T_{\beta_1}$ where $T_{\beta_1} : \mathbb{R}^{c \times d \times d} \rightarrow \mathbb{R}^{c' \times d' \times d'}$ and $T_{\beta_2} : \mathbb{R}^{c' \times d' \times d'} \rightarrow \mathbb{R}$. In greater detail, T_{β_1} maps the original images to their corresponding features maps and T_{β_2} maps their features maps to their corresponding discriminative scores. Let the data

Table 1: Values of SW and CSW variants between probability measures over digits images on MNIST with $L = 100$

		0	1	2	3	4	5	6	7	8	9
0	SW	0.58±0.01	23.19±0.88	15.81±0.88	15.31±0.83	17.25±0.57	12.45±0.91	16.44±0.8	17.71±0.71	15.8±1.12	18.14±0.94
	CSW-b	0.83±0.03	32.33±3.02	24.86±2.11	25.73±2.43	24.71±2.55	18.6±1.76	21.86±1.71	25.6±1.72	27.24±2.36	24.93±0.92
	CSW-s	0.59±0.04	24.13±2.36	16.95±1.21	15.21±2.02	19.2±1.33	13.33±1.85	18.0±1.57	18.04±2.21	15.51±2.21	17.99±2.64
	CSW-d	0.59±0.01	22.65±1.47	16.15±1.28	16.79±0.79	17.91±0.65	12.6±1.28	17.81±1.28	18.53±1.54	14.85±1.76	16.93±0.97
1	SW	22.36±0.92	0.45±0.0	16.48±1.24	16.26±0.48	16.58±0.79	15.53±0.37	16.95±1.04	15.71±0.8	14.59±0.45	15.82±0.67
	CSW-b	34.71±1.82	0.65±0.02	24.19±2.05	25.62±1.61	27.75±1.6	23.7±1.92	28.07±0.58	27.05±2.75	23.84±1.37	25.44±0.93
	CSW-s	22.59±3.07	0.45±0.03	16.04±1.25	17.2±0.8	16.25±1.13	15.7±1.3	17.37±1.37	15.87±0.76	15.85±0.96	17.08±0.96
	CSW-d	23.48±1.47	0.46±0.01	16.41±0.73	16.39±0.74	16.93±0.99	15.01±0.74	16.85±1.02	16.48±0.99	15.22±0.78	15.76±0.8
2	SW	16.03±0.84	16.4±0.29	0.62±0.02	12.9±0.53	12.98±1.39	12.83±0.39	11.11±0.31	16.41±0.54	11.35±0.79	14.61±0.75
	CSW-b	26.62±1.65	24.57±1.05	0.89±0.05	19.56±1.07	19.09±0.48	20.65±1.91	17.95±0.94	20.9±1.96	16.98±1.21	18.81±0.66
	CSW-s	16.38±1.76	16.3±0.87	0.64±0.03	11.92±0.89	14.81±2.17	11.42±1.09	11.3±0.85	15.27±1.29	10.58±1.38	14.84±2.31
	CSW-d	16.22±0.98	17.09±0.93	0.6±0.01	13.22±0.37	13.81±0.73	11.92±0.5	12.13±1.0	16.3±0.93	11.82±1.26	15.26±1.45
3	SW	15.89±0.82	15.7±0.63	12.6±0.96	0.57±0.01	15.04±0.93	8.89±0.57	14.96±1.34	14.8±0.46	9.85±0.62	13.52±0.77
	CSW-b	26.62±1.65	25.43±3.13	18.57±1.66	0.87±0.05	22.38±2.45	14.11±1.52	23.83±2.36	24.15±1.44	17.0±1.84	19.68±1.21
	CSW-s	16.71±1.88	16.25±1.41	12.31±1.55	0.6±0.01	13.7±0.91	8.97±1.41	15.69±1.04	14.94±1.41	10.91±0.63	14.07±1.26
	CSW-d	15.23±1.83	16.37±1.05	13.19±0.79	0.58±0.02	15.0±0.91	9.21±0.61	16.14±0.32	15.64±1.24	11.1±0.76	13.93±0.6
4	SW	17.02±1.0	16.82±0.86	12.61±0.55	14.75±0.99	0.58±0.01	11.39±0.44	12.07±0.51	10.51±0.56	12.43±0.78	6.78±0.47
	CSW-b	26.86±2.04	26.44±1.75	18.91±2.74	22.08±1.47	0.83±0.03	18.51±1.15	18.49±1.35	18.95±1.67	17.29±2.19	10.54±0.69
	CSW-s	16.2±2.1	15.65±1.16	13.94±1.92	15.23±1.32	0.58±0.03	11.29±2.18	12.33±1.05	11.07±0.9	12.39±1.71	7.84±0.79
	CSW-d	17.34±1.77	17.28±1.27	13.08±1.54	15.3±0.67	0.57±0.01	12.0±0.52	13.23±0.44	11.98±0.71	11.39±0.75	7.26±0.51
5	SW	11.77±0.36	14.55±0.93	12.64±0.47	8.7±0.71	10.68±1.3	0.64±0.01	11.83±0.83	12.54±0.2	8.99±0.78	10.4±0.75
	CSW-b	20.55±1.98	25.31±2.14	19.68±0.92	13.55±1.5	18.43±1.22	0.91±0.02	16.55±1.0	17.45±0.8	14.4±1.07	15.85±1.21
	CSW-s	13.04±0.61	15.15±1.18	12.65±0.94	8.27±1.01	11.83±0.85	0.62±0.01	12.04±1.0	12.36±1.48	8.64±0.55	10.8±0.97
	CSW-d	11.79±1.28	15.31±1.15	13.54±1.22	8.82±1.07	12.33±0.75	0.62±0.04	12.45±0.79	13.02±0.81	9.18±0.54	10.73±0.85
6	SW	15.97±0.87	16.84±1.4	11.52±0.53	15.56±0.66	12.09±0.63	11.98±0.82	0.65±0.01	16.69±1.63	12.52±0.42	13.84±0.93
	CSW-b	25.66±2.37	26.39±0.68	15.93±0.91	22.98±3.47	18.8±1.9	17.0±1.66	0.91±0.02	23.31±2.45	17.62±0.99	18.73±0.84
	CSW-s	17.84±1.85	17.61±1.92	11.49±0.42	14.07±1.43	12.25±1.23	11.74±0.35	0.66±0.01	15.71±1.03	13.33±0.68	12.55±1.4
	CSW-d	16.95±1.45	17.15±1.12	11.47±0.79	15.71±1.24	11.91±0.37	12.63±0.94	0.67±0.02	16.36±1.29	13.15±1.0	14.35±0.92
7	SW	17.55±1.35	16.65±0.79	15.3±0.83	15.47±0.73	11.39±0.77	12.4±0.54	16.04±1.19	0.61±0.01	13.66±1.12	8.16±0.06
	CSW-b	27.36±2.01	28.35±1.32	22.24±1.59	23.56±1.2	18.46±2.75	19.32±1.68	25.38±1.94	0.94±0.04	22.63±1.67	14.71±0.52
	CSW-s	16.74±2.14	15.81±1.23	17.72±2.26	14.75±0.83	13.6±2.24	13.45±1.94	15.37±1.44	0.64±0.05	12.92±0.77	8.95±1.3
	CSW-d	18.21±1.44	16.31±1.55	16.3±1.05	14.97±0.76	11.45±0.35	12.82±1.54	16.9±0.95	0.69±0.04	13.3±0.59	8.72±0.48
8	SW	16.16±1.14	15.09±0.96	11.02±0.54	10.02±0.79	11.45±0.69	8.46±0.75	13.41±0.29	14.33±1.27	0.65±0.02	10.62±0.35
	CSW-b	26.49±2.12	21.76±0.63	15.73±1.07	17.16±1.58	18.25±1.36	14.5±0.94	18.87±1.68	21.36±1.76	0.97±0.04	15.85±0.81
	CSW-s	17.19±1.17	14.26±1.07	11.01±0.79	10.32±1.02	11.86±1.4	8.75±0.63	13.23±0.96	13.72±1.3	0.66±0.04	10.65±1.02
	CSW-d	15.42±1.31	15.41±0.87	11.06±0.43	10.56±0.44	12.51±1.74	8.98±0.61	13.87±1.29	14.77±0.67	0.65±0.03	11.09±1.06
9	SW	17.94±1.19	15.68±0.64	13.83±1.05	12.72±0.48	7.37±0.66	10.62±0.92	13.54±0.48	8.24±0.31	10.66±0.38	0.59±0.02
	CSW-b	26.67±3.65	26.0±1.95	20.52±1.24	19.68±1.14	10.39±0.42	16.36±2.03	19.24±0.99	14.95±1.29	15.71±1.44	0.84±0.04
	CSW-s	16.73±1.84	16.04±1.28	14.31±1.66	13.22±1.43	7.42±0.45	10.32±0.65	13.74±2.08	8.64±0.8	10.52±1.33	0.6±0.02
	CSW-d	17.58±1.17	15.43±1.09	13.98±0.51	13.55±1.43	7.18±0.37	10.89±0.58	13.94±1.11	8.58±0.42	11.68±0.62	0.6±0.02

distribution is μ , our training objectives are:

$$\min_{\beta_1, \beta_2} (\mathbb{E}_{x \sim \mu} [\min(0, -1 + T_{\beta_2}(T_{\beta_1}(x)))] + \mathbb{E}_{z \sim \epsilon} [\min(0, -1 - T_{\beta_2}(T_{\beta_1}(G_\phi(z))))]),$$

$$\min_{\phi} \mathbb{E}_{X \sim \mu^{\otimes m}, Y \sim \epsilon^{\otimes m}} \mathcal{D}(T_{\beta_1} \# P_X, T_{\beta_1} \# G_\phi \# P_Y),$$

where $m \geq 1$ is the mini-batch size and $\mathcal{D}(\cdot, \cdot)$ is the SW or CSW's variants.

We train the above model on standard benchmarks such as CIFAR10 (32x32) [26], STL10 (96x96) [8], CelebA (64x64), and CelebAHQ (128x128) [36]. To compare models, we use the FID score [19] and the Inception score (IS) [50]. The detailed settings about architectures, hyperparameters, and evaluation of FID and IS are given in Appendix D. We first show the FID scores and IS scores of generative models trained by SW and CSW's variants with the number of projections $L \in \{1, 100, 100\}$ in Table 2. In the table, we report the performance of models at the last training

Table 2: Summary of FID and IS scores of methods on CIFAR10 (32x32), CelebA (64x64), STL10 (96x96), and CelebA-HQ (128x128).

Method	CIFAR10 (32x32)		CelebA (64x64)	STL10 (96x96)		CelebA-HQ (128x128)
	FID (\downarrow)	IS (\uparrow)	FID (\downarrow)	FID (\downarrow)	IS (\uparrow)	FID (\downarrow)
SW (L=1)	87.97	3.59	128.81	170.96	3.68	275.44
CSW-b (L=1)	84.38	4.28	85.83	173.33	3.89	315.91
CSW-s (L=1)	80.10	4.31	66.52	168.93	3.75	303.57
CSW-d (L=1)	63.94	4.89	89.37	212.61	2.48	321.06
SW (L=100)	53.67	5.74	20.08	100.35	8.14	51.80
CSW-b (L=100)	49.78	5.78	18.96	91.75	8.11	53.05
CSW-s (L=100)	43.88	6.13	13.76	97.08	8.20	32.94
CSW-d (L=100)	47.16	5.90	14.96	102.58	7.53	41.01
SW (L=1000)	43.11	6.09	14.92	84.78	9.06	28.19
CSW-b (L=1000)	43.17	6.07	14.75	86.98	9.11	29.69
CSW-s (L=1000)	35.40	6.64	12.55	77.24	9.31	22.25
CSW-d (L=1000)	41.34	6.33	13.24	83.36	9.42	25.93

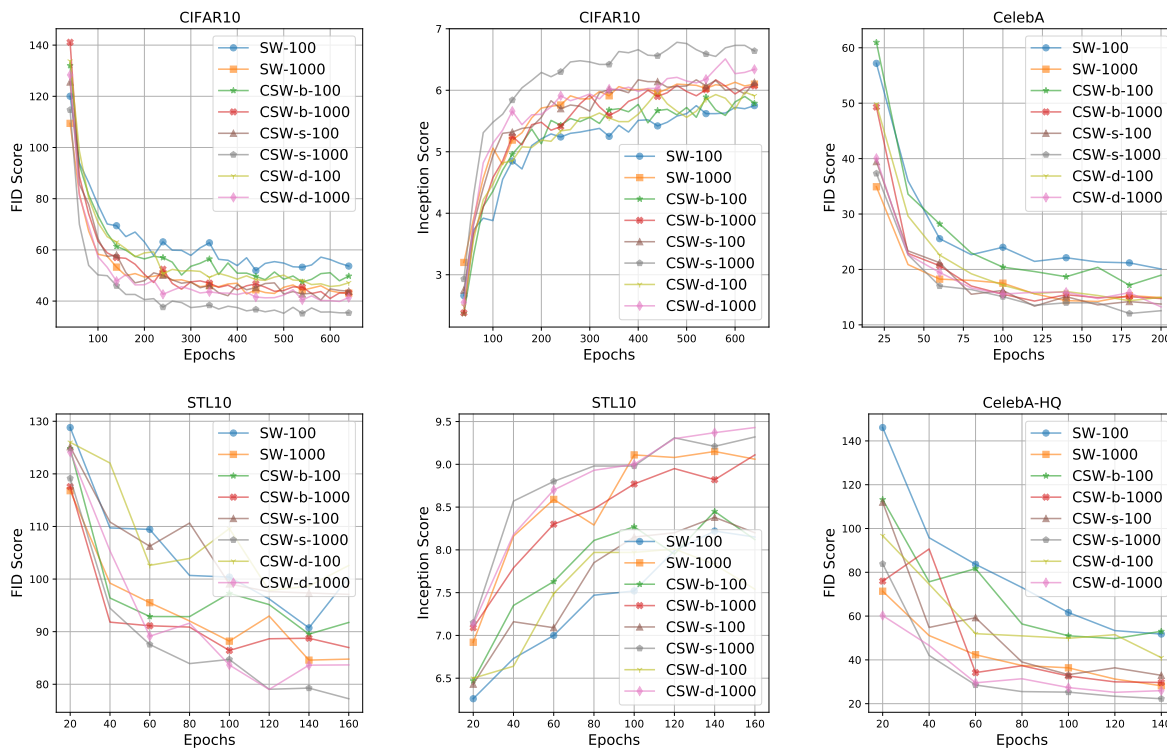


Figure 3: FID scores and IS scores over epochs of different training losses on datasets. We observe that CSW’s variants usually help the generative models converge faster.

epoch. We do not report the IS scores on CelebA and CelebA-HQ since the IS scores are not suitable for face images. We then demonstrate the FID scores and IS scores across training epochs in Figure 3 for investigating the convergence of generative models trained by SW and CSW’s variants. After

Table 3: Computational time and memory of methods (reported in the number of iterations per a second and megabytes (MB)).

Method	CIFAR10 (32x32)		CelebA (64x64)		STL10 (96x96)		CelebA-HQ (128x128)	
	Iters/s (\uparrow)	Mem (\downarrow)	Iters/s (\uparrow)	Mem (\downarrow)	Iters/s (\uparrow)	Mem (\downarrow)	Iters/s (\uparrow)	Mem (\downarrow)
SW ($L=1$)	18.98	2071	6.21	8003	9.59	4596	10.35	4109
SW ($L=100$)	18.53	2080	6.16	8015	9.47	4601	10.22	4117
SW ($L=1000$)	18.15	2169	6.10	8102	9.13	4647	10.17	4202
CSW-b ($L=1$)	18.43	2070	6.21	8003	9.56	4596	10.33	4109
CSW-b ($L=100$)	18.35	2077	6.15	8009	9.40	4598	10.19	4110
CSW-b ($L=1000$)	18.06	2117	6.10	8049	9.07	4613	10.12	4134
CSW-s (d) ($L=1$)	18.69	2070	6.21	8003	9.56	4596	10.33	4109
CSW-s (d) ($L=100$)	18.50	2073	6.16	8005	9.41	4597	10.20	4109
CSW-s (d) ($L=1000$)	18.10	2098	6.10	8029	9.10	4603	10.12	4114



Figure 4: Random generated images of SW and CSW-s on CIFAR10.

that, we report the training time and training memory of SW and CSW variants in Table 3. Finally, we show some randomly generated images from SW’s models and CSW-s’ models in Figures 4-7. Additional experimental results with CSW-b and CSW-d are given in Appendix C.

Summary of FID scores and IS scores: According to Table 2, on CIFAR10, CSW-d gives the lowest values of FID scores and IS scores when $L = 1$ while CSW-s gives the lowest FID scores when $L = 100$ and $L = 1000$. Compared to CSW-s, CSW-d and CSW yield higher FID scores and lower IS scores. However, CSW-d and CSW are still better than SW. On CelebA, CSW-s perform the best in all settings. On STL10, CSW’s variants are also better than the vanilla SW, however,



Figure 5: Random generated images of SW and CSW-s on CelebA.

it is hard to figure out which is the best variant. On CelebA-HQ, SW gives the lowest FID score when $L = 1$. In contrast, when $L = 100$ and $L = 1000$, CSW-s is the best choice for training the generative model. Since the FID scores of $L = 1$ are very high on CelebA-HQ and STL10, the scores are not very meaningful for comparing SW and CSW’s variants. For all models, increasing L leads to better generative quality. Overall, we observe that CSW’s variants enhance the performance of the generative models well.

FID scores and IS scores across epochs: From Figure 3, we observe that CSW’s variants help the generative models converge faster than SW when $L = 100$ and $L = 1000$. Increasing the number of projections from 100 to 1000, the generative models from both SW and CSW’s variants become better. Overall, CSW-s is the best option for training generative models among CSW’s variants since its FID curves are the lowest and its IS curves are the highest.

Training time and training memory: We report in Table 3 the training speed in the number of iterations per second and the training memory in megabytes (MBs). We would like to recall that the time complexity and the projection memory complexity of CSW-s and CSW-d are the same. Therefore, we measure the training time and the training memory of CSW-s as the result for both CSW-s and CSW-d. We can see that increasing the number of projections L costs more memory and also slows down the training speed. However, the rate of increasing memory of CSW is smaller than SW. For CSW-s and CSW-d, the extent of saving memory is even better. As an example, $L = 1000$ in CSW-s and CSW-d costs less memory than SW with $L = 100$ while the performance is better (see Table 2). In terms of training time, CSW-s and CSW-d are comparable to SW and they can be computed faster than CSW. We refer the readers to Section 3 for a detailed discussion about the computational time and projection memory complexity of CSW’s variants.

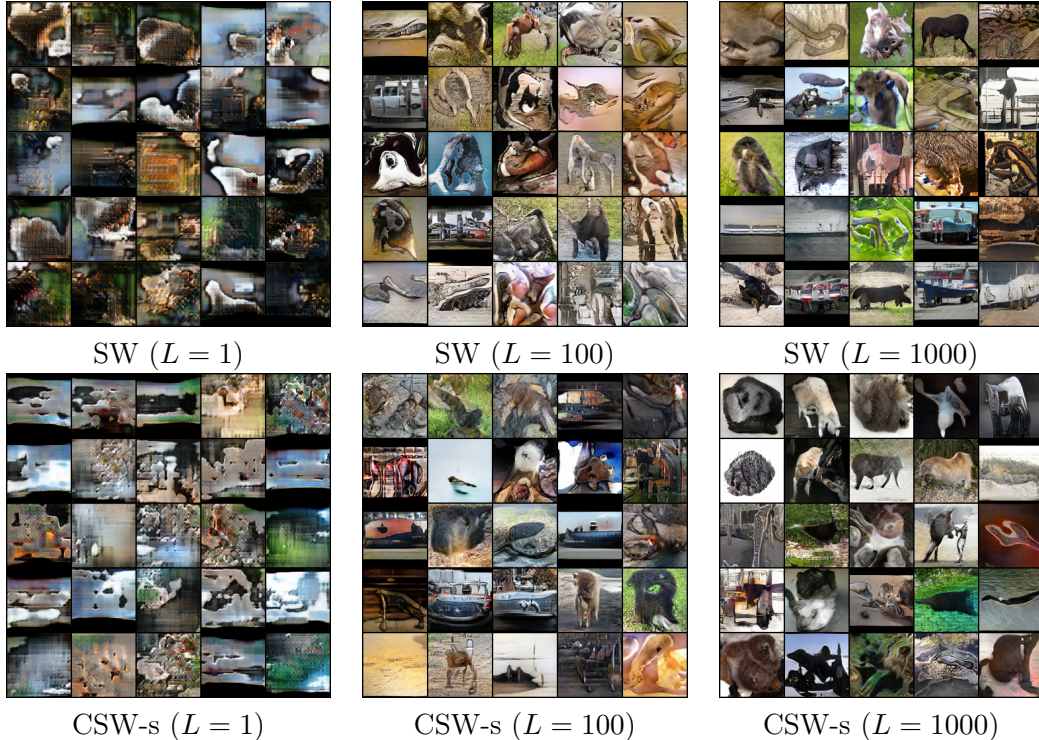


Figure 6: Random generated images of SW and CSW-s on STL10.

Generated images: We show randomly generated images on CIFAR10, CelebA, STL10, and CelebA-HQ in Figures 4-7 as qualitative comparison between SW and CSW-s. From the figures, we can see that generated images of CSW-s is more realistic than ones of SW. The difference is visually clear when the number of projections L is small e.g., $L = 1$ and $L = 100$. When $L = 1000$, we can still figure out that CSW-s is better than SW by looking at the sharpness of the generated images. Also, we can visually observe the improvement of SW and CSW-s when increasing the number of projections. In summary, the qualitative results are consistent with the quantitative results (FID scores and IS scores) in Table 2. For the generated images of CSW-b and CSW-d, we show them in Figures 8-11.

Non-linear convolution sliced Wasserstein: We also compare non-linear extensions of SW and CSW variants in training generative models on CIFAR10 in Appendix C. For details of non-linear extensions, we refer to Appendix B. From experiments, we observe that convolution can also improve the performance of sliced Wasserstein in non-linear projecting cases. Compared to linear versions, non-linear versions can enhance the quality of the generative model or yield comparable results.

6 Conclusion

We have addressed the issue of the conventional slicing process of sliced Wasserstein when working with probability measures over images. In particular, sliced Wasserstein is defined on probability measures over vectors which leads to the step of vectorization for images. As a result, the conventional slicing process cannot exploit the spatial structure of data for designing the space of projecting directions and projecting operators. To address the issue, we propose a new slicing process by



Figure 7: Random generated images of SW and CSW-s on CelebA-HQ.

using the convolution operator which has been shown to be efficient on images. Moreover, we investigate the computational complexity and projection memory complexity of the new slicing technique. We show that convolution slicing is comparable to conventional slicing in terms of computational complexity while being better in terms of projection memory complexity. By utilizing the new slicing technique, we derive a novel family of sliced Wasserstein variants, named convolution sliced Wasserstein. We investigate the properties of the convolution sliced Wasserstein including its metricity, its computational and sample complexities, and its connection to other variants of sliced Wasserstein in literature. Finally, we carry out extensive experiments in comparing digits images and training generative models on standard benchmark datasets to demonstrate the favorable performance of the convolution sliced Wasserstein.

Supplement to "Revisiting Sliced Wasserstein on Images: From Vectorization to Convolution"

In this supplement, we collect the materials that are deferred from the main text. In Appendix [A](#), we provide proofs for key results in the paper. In Appendix [B](#), we introduce non-linear versions of the convolution sliced Wasserstein. In Appendix [C](#), we include additional experiments for comparing measures over MNIST's digits via sliced Wasserstein and convolution sliced Wasserstein. We further provide generated images for convolution sliced Wasserstein with convolution-base and convolution-dilation slicers under generative models settings. Finally, in Appendix [D](#), we include details of

experimental settings in the paper.

A Proofs

In this appendix, we provide proofs for key results in the main text.

A.1 Proof of Theorem 1

For any $p \geq 1$, it is clear that when $\mu = \nu$, then $\text{CSW}_p(\mu, \nu) = 0$. Furthermore, $\text{CSW}_p(\mu, \nu) = \text{CSW}_p(\nu, \mu)$ for any probability measures μ and ν . Therefore, to obtain the conclusion of the theorem, it is sufficient to demonstrate that it satisfies the triangle inequality. Indeed, for any probability measures μ_1, μ_2, μ_3 , we find that

$$\begin{aligned}
& \text{CSW}_p(\mu_1, \mu_3) \\
&= \left(\mathbb{E}_{K^{(1)} \sim \mathcal{U}(\mathcal{K}^{(1)}), \dots, K^{(N)} \sim \mathcal{U}(\mathcal{K}^{(N)})} \left[W_p^p \left(\mathcal{S}(\cdot | K^{(1)}, \dots, K^{(N)}) \# \mu_1, \mathcal{S}(\cdot | K^{(1)}, \dots, K^{(N)}) \# \mu_3 \right) \right] \right)^{\frac{1}{p}} \\
&\leq \left(\mathbb{E}_{K^{(1)} \sim \mathcal{U}(\mathcal{K}^{(1)}), \dots, K^{(N)} \sim \mathcal{U}(\mathcal{K}^{(N)})} \left[W_p \left(\mathcal{S}(\cdot | K^{(1)}, \dots, K^{(N)}) \# \mu_1, \mathcal{S}(\cdot | K^{(1)}, \dots, K^{(N)}) \# \mu_2 \right) \right. \right. \\
&\quad \left. \left. + W_p \left(\mathcal{S}(\cdot | K^{(1)}, \dots, K^{(N)}) \# \mu_2, \mathcal{S}(\cdot | K^{(1)}, \dots, K^{(N)}) \# \mu_3 \right) \right]^p \right)^{1/p} \\
&\leq \left(\mathbb{E}_{K^{(1)} \sim \mathcal{U}(\mathcal{K}^{(1)}), \dots, K^{(N)} \sim \mathcal{U}(\mathcal{K}^{(N)})} \left[W_p^p \left(\mathcal{S}(\cdot | K^{(1)}, \dots, K^{(N)}) \# \mu_1, \mathcal{S}(\cdot | K^{(1)}, \dots, K^{(N)}) \# \mu_2 \right) \right] \right)^{1/p} \\
&+ \left(\mathbb{E}_{K^{(1)} \sim \mathcal{U}(\mathcal{K}^{(1)}), \dots, K^{(N)} \sim \mathcal{U}(\mathcal{K}^{(N)})} \left[W_p^p \left(\mathcal{S}(\cdot | K^{(1)}, \dots, K^{(N)}) \# \mu_2, \mathcal{S}(\cdot | K^{(1)}, \dots, K^{(N)}) \# \mu_3 \right) \right] \right)^{1/p} \\
&= \text{CSW}_p(\mu_1, \mu_2) + \text{CSW}_p(\mu_2, \mu_3),
\end{aligned}$$

where the first inequality is due to the triangle inequality with Wasserstein metric, namely, we have

$$\begin{aligned}
W_p \left(\mathcal{S}(\cdot | K^{(1)}, \dots, K^{(N)}) \# \mu_1, \mathcal{S}(\cdot | K^{(1)}, \dots, K^{(N)}) \# \mu_3 \right) &\leq W_p \left(\mathcal{S}(\cdot | K^{(1)}, \dots, K^{(N)}) \# \mu_1, \mathcal{S}(\cdot | K^{(1)}, \dots, K^{(N)}) \# \mu_2 \right) \\
&+ W_p \left(\mathcal{S}(\cdot | K^{(1)}, \dots, K^{(N)}) \# \mu_2, \mathcal{S}(\cdot | K^{(1)}, \dots, K^{(N)}) \# \mu_3 \right)
\end{aligned}$$

while the second inequality is an application of Minkowski inequality for integrals. As a consequence, we obtain the conclusion of the theorem.

A.2 Proof of Proposition 2

The proof of this proposition is direct from the definition of the convolution sliced Wasserstein. Here, we provide the proof for the completeness. Indeed, since the convolution slicer $\mathcal{S}(\cdot | K^{(1)}, \dots, K^{(N)})$

is a mapping from $\mathbb{R}^{c \times d \times d}$ to \mathbb{R} , it is clear that

$$\begin{aligned}
& \text{CSW}_p(\mu, \nu) \\
&= \left(\mathbb{E}_{K^{(1)} \sim \mathcal{U}(\mathcal{K}^{(1)}), \dots, K^{(N)} \sim \mathcal{U}(\mathcal{K}^{(N)})} \left[W_p^p \left(\mathcal{S}(\cdot | K^{(1)}, \dots, K^{(N)}) \# \mu, \mathcal{S}(\cdot | K^{(1)}, \dots, K^{(N)}) \# \nu \right) \right] \right)^{\frac{1}{p}} \\
&\leq \max_{K^{(i)} \in \mathbb{R}^{c^{(1)} \times d^{(i)} \times d^{(i)}} \forall i \in [N]} W_p \left(\mathcal{S}(\cdot | K^{(1)}, \dots, K^{(N)}) \# \mu, \mathcal{S}(\cdot | K^{(1)}, \dots, K^{(N)}) \# \nu \right) \\
&\leq \max_{\theta \in \mathbb{R}^{cd^2}: \|\theta\| \leq 1} W_p(\theta \# \mu, \theta \# \nu) = \text{max-SW}_p(\mu, \nu),
\end{aligned}$$

where the second inequality is due to the inequality with ℓ_2 norm of convolution of matrices and the fact that the ℓ_2 norm of each tensor $K^{(i)}$ is 1 for all $i \in [N]$. In addition, we find that

$$\begin{aligned}
\text{max-SW}_p^p(\mu, \nu) &= \max_{\theta \in \mathbb{R}^{cd^2}: \|\theta\| \leq 1} \left(\inf_{\pi \in \Pi(\mu, \nu)} \int_{\mathbb{R}^{cd^2}} |\theta^\top x - \theta^\top y|^p d\pi(x, y) \right) \\
&\leq \max_{\theta \in \mathbb{R}^{cd^2}: \|\theta\| \leq 1} \left(\inf_{\pi \in \Pi(\mu, \nu)} \int_{\mathbb{R}^{cd^2} \times \mathbb{R}^{cd^2}} \|\theta\|^p \|x - y\|^p d\pi(x, y) \right) \\
&\leq \inf_{\pi \in \Pi(\mu, \nu)} \int_{\mathbb{R}^{cd^2} \times \mathbb{R}^{cd^2}} \|\theta\|^p \|x - y\|^p d\pi(x, y) = W_p^p(\mu, \nu).
\end{aligned}$$

Putting the above results together, we obtain the conclusion of the proposition.

A.3 Proof of Proposition 3

From the assumption of Proposition 3, we denote $\Theta \subset \mathbb{R}^{c \times d \times d}$ as the compact set that the probability measure P is supported on. Based on the result of Proposition 2, we have

$$\mathbb{E}[\text{CSW}_p(P_n, P)] \leq \mathbb{E}[\text{max-SW}_p(P_n, P)],$$

where $\text{max-SW}_p(P_n, P) = \max_{\theta \in \mathbb{R}^{cd^2}: \|\theta\| \leq 1} W_p(\theta \# P_n, \theta \# P)$. Therefore, to obtain the conclusion of the proposition, it is sufficient to demonstrate that $\mathbb{E}[\text{max-SW}_p(P_n, P)] \leq C \sqrt{(cd^2 + 1) \log_2 n/n}$ for some universal constant $C > 0$. Indeed, from the closed-form expression of Wasserstein metric in one dimension, we have

$$\begin{aligned}
\text{max-SW}_p^p(P_n, P) &= \max_{\theta \in \mathbb{R}^{cd^2}: \|\theta\| \leq 1} \int_0^1 |F_{n, \theta}^{-1}(u) - F_\theta^{-1}(u)|^p du \\
&= \max_{\theta \in \mathbb{R}^{cd^2}: \|\theta\| \leq 1} \int_{\mathbb{R}} |F_{n, \theta}(x) - F_\theta(x)|^p dx, \quad \leq \text{diam}(\Theta) \max_{\theta \in \mathbb{R}^{cd^2}: \|\theta\| \leq 1} |F_{n, \theta}(x) - F_\theta(x)|^p,
\end{aligned}$$

where $F_{n, \theta}$ and F_θ are respectively the cumulative distributions of $\theta \# P_n$ and $\theta \# P$. Furthermore, we have the following relation:

$$\max_{\theta \in \mathbb{R}^{cd^2}: \|\theta\| \leq 1} |F_{n, \theta}(x) - F_\theta(x)| = \sup_{A \in \mathcal{A}} |P_n(A) - P(A)|,$$

where \mathcal{A} is the set of half-spaces $\{y \in \mathbb{R}^{cd^2} : \theta^\top y \leq x\}$ for all $\theta \in \mathbb{R}^{cd^2}$ such that $\|\theta\| \leq 1$. The Vapnik-Chervonenkis (VC) dimension of \mathcal{A} is upper bounded by $cd^2 + 1$ (see the reference [54]).

Therefore, with probability at least $1 - \delta$ we obtain that

$$\sup_{A \in \mathcal{A}} |P_n(A) - P(A)| \leq \sqrt{\frac{32}{n} [(cd^2 + 1) \log_2(n + 1) + \log_2(8/\delta)]}.$$

Putting the above results together, we can conclude that $\mathbb{E}[\max\text{-SW}_p(P_n, P)] \leq C \sqrt{(cd^2 + 1) \log_2 n/n}$ for some universal constant $C > 0$. As a consequence, we obtain the conclusion of the proposition.

A.4 Proof of Proposition 1

(a) We first consider the computational and projection memory complexities of the convolution-base slicer. When d is even, we can write down $d = 2^{\lfloor \log_2 d \rfloor - 1} \cdot \frac{d}{2^{\lfloor \log_2 d \rfloor - 1}}$. Direct calculation indicates that the computational complexity of convolution-base slicer is

$$\begin{aligned} & \mathcal{O} \left(\frac{d^2}{4} \cdot c \left(\frac{d}{2} + 1 \right)^2 + \left(\sum_{l=2}^{\lfloor \log_2 d \rfloor - 1} (2^{-l}d)^2 (2^{-l}d + 1)^2 \right) + \frac{d^2}{4^{\lfloor \log_2 d \rfloor - 1}} \right) \\ &= \mathcal{O} \left(\frac{cd^4}{16} + d^4 \sum_{l=2}^{\lfloor \log_2 d \rfloor - 1} \frac{1}{16^l} \right) \\ &= \mathcal{O} \left(\frac{cd^4}{16} - d^4 - \frac{d^4}{16} + \sum_{l=0}^{\lfloor \log_2 d \rfloor - 1} \frac{1}{16^l} \right) \\ &= \frac{cd^4}{16} + \frac{d^2}{4^{\lfloor \log_2 d \rfloor}} - d^4 - \frac{d^4}{16} + d^4 \frac{1 - \frac{1}{16^{\lfloor \log_2 d \rfloor}}}{1 - \frac{1}{16}} \\ &= \mathcal{O} \left(\left(\frac{c - 17}{16} + \frac{16^{\lfloor \log_2 d \rfloor} - 1}{15 \cdot 16^{\lfloor \log_2 d \rfloor - 1}} \right) d^4 \right) = \mathcal{O}(cd^4). \end{aligned}$$

Similarly, we can check that the projection memory complexity of convolution-base slicer is

$$\begin{aligned} & \mathcal{O} \left(\frac{cd^2}{4} + \left(\sum_{l=2}^{\lfloor \log_2 d \rfloor - 1} (2^{-l}d)^2 \right) + \frac{d^2}{4^{\lfloor \log_2 d \rfloor - 1}} \right) = \mathcal{O} \left(\frac{cd^2}{4} + \frac{d^2}{4^{\lfloor \log_2 d \rfloor}} - d^2 + d^2 \frac{1 - \frac{1}{4^{\lfloor \log_2 d \rfloor}}}{1 - \frac{1}{4}} \right) \\ &= \mathcal{O} \left(\left(\frac{c - 5}{4} + \frac{4^{\lfloor \log_2 d \rfloor} - 1}{3 \cdot 4^{\lfloor \log_2 d \rfloor - 1}} \right) d^2 \right) = \mathcal{O}(cd^2). \end{aligned}$$

Therefore, we obtain the conclusion of part (a) when d is even. Moving to the case when d is odd, the computational complexity of convolution-base slicer becomes

$$\begin{aligned} & \mathcal{O} \left(4c \cdot (d-1)^2 + \frac{(d-1)^4}{16} + \frac{(d-1)^2}{4^{\lfloor \log_2(d-1) \rfloor - 1}} - (d-1)^4 - \frac{(d-1)^4}{16} + (d-1)^4 \frac{1 - \frac{1}{16^{\lfloor \log_2(d-1) \rfloor}}}{1 - \frac{1}{16}} \right) \\ &= \mathcal{O} \left(4cd^2 + \left(\frac{16^{\lfloor \log_2(d-1) \rfloor} - 1}{15 \cdot 16^{\lfloor \log_2(d-1) \rfloor - 1}} - \frac{17}{16} \right) d^4 \right) = \mathcal{O}(cd^2 + d^4). \end{aligned}$$

Similarly, we can check that when d is odd, the projection memory complexity of convolution-base slicer is $\mathcal{O}\left(4c + \left(\frac{4^{\lceil \log_2(d-1) \rceil} - 1}{3 \cdot 4^{\lceil \log_2(d-1) \rceil - 1}} - \frac{5}{4}\right) d^2\right) = \mathcal{O}(cd^2)$. As a consequence, we obtain our claims with the computational and projection memory complexities of convolution-base slicer.

(b) We now establish the computational and projection memory complexities of convolution-stride slicer. When d is even, we can write down $d = 2^{\lceil \log_2 d \rceil - 1} \cdot \frac{d}{2^{\lceil \log_2 d \rceil - 1}}$. Then, the computational complexity of convolution-stride slicer is

$$\begin{aligned} \mathcal{O}\left(4c \cdot \frac{d^2}{4} + \left(\sum_{l=2}^{\lceil \log_2 d \rceil - 1} 4(2^{-l}d)^2\right) + \frac{d^2}{4^{\lceil \log_2 d \rceil - 1}}\right) &= \mathcal{O}\left(cd^2 + 4d^2\left(-1 - \frac{1}{4} + \frac{1 - \frac{1}{4^{\lceil \log_2 d \rceil}}}{1 - \frac{1}{4}}\right)\right) \\ &= \mathcal{O}\left(\left(\frac{c-5}{4} + \frac{4^{\lceil \log_2 d \rceil} - 1}{3 \cdot 4^{\lceil \log_2 d \rceil - 1}}\right) d^2\right). \end{aligned}$$

Similarly, the projection memory complexity of convolution-stride slicer is

$$\mathcal{O}\left(4c + \left(\sum_{l=2}^{\lceil \log_2 d \rceil - 1} 4\right) + \frac{d^2}{4^{\lceil \log_2 d \rceil - 1}}\right) = \mathcal{O}\left(4c + \frac{d^2}{4^{\lceil \log_2 d \rceil - 1}} + 4\lceil \log_2 d \rceil\right) = \mathcal{O}(c + \lceil \log_2 d \rceil).$$

When d is odd, the computational complexity of convolution-stride slicer is

$$\begin{aligned} \mathcal{O}\left(4c \cdot (d-1)^2 + 4\frac{(d-1)^2}{4} + \left(\sum_{l=2}^{\lceil \log_2(d-1) \rceil - 1} 4(2^{-l}(d-1))^2\right) + \frac{(d-1)^2}{4^{\lceil \log_2(d-1) \rceil - 1}}\right) \\ = \mathcal{O}\left(4c(d-1)^2 + 4d^2\left(-1 - \frac{1}{4} + \frac{1 - \frac{1}{4^{\lceil \log_2(d-1) \rceil}}}{1 - \frac{1}{4}}\right)\right) \\ = \mathcal{O}\left(\left(4c + \frac{4^{\lceil \log_2(d-1) \rceil} - 1}{3 \cdot 4^{\lceil \log_2(d-1) \rceil - 1}} - \frac{5}{4}\right) d^2\right) := \mathcal{O}(cd^2). \end{aligned}$$

Similarly, we can check that when d is odd, the projection memory complexity of convolution-stride slicer is $\mathcal{O}\left(4c + \frac{(d-1)^2}{4^{\lceil \log_2(d-1) \rceil - 1}} + 4\lceil \log_2(d-1) \rceil\right) = \mathcal{O}(c + \lceil \log_2 d \rceil)$. As a consequence, we obtain the conclusion of part (b).

(c) Since the convolution-dilation slicer is designed in the same way as that of the convolution-stride slicer, its computational complexity and projection memory complexity can be derived in the same manner as those of the convolution-stride slicer. As a consequence, we reach the conclusion of part (c).

B Non-linear Versions of Convolution Sliced Wasserstein

In this appendix, we consider an extension of convolution sliced Wasserstein to non-linear convolution sliced Wasserstein to enhance the ability of convolution sliced Wasserstein to capture the non-linearity of the data. We first state the definition of non-linear convolution-base slicer.

Definition 7. (*Non-Linear Convolution-base Slicer*) Given $X \in \mathbb{R}^{c \times d \times d}$ ($d \geq 2$) and a non linear activation $\sigma(\cdot)$,

Table 4: Values of SW and CSW’s variants between probability measures over digits images on MNIST with $L = 1$.

	0	1	2	3	4	5	6	7	8	9	
0	SW	0.59±0.12	9.4±3.33	8.83±5.14	12.34±10.13	14.61±8.93	4.43±2.4	10.3±5.61	7.89±3.39	10.37±7.68	15.92±6.76
	CSW-b	0.68±0.23	38.28±7.75	15.9±7.74	30.9±27.25	20.35±11.8	19.76±13.07	14.54±4.88	14.88±9.95	17.34±7.05	31.51±27.5
	CSW-s	0.42±0.22	18.3±11.06	12.57±10.71	13.41±12.62	30.13±13.13	8.85±4.24	6.8±4.31	7.4±5.0	11.24±11.9	25.05±22.1
	CSW-d	0.62±0.44	19.56±8.64	9.91±6.38	11.34±4.58	12.72±7.89	5.18±1.56	10.94±5.28	6.39±3.4	9.51±8.21	8.06±4.92
1	SW	18.23±12.47	0.32±0.08	8.86±3.11	13.46±4.29	10.87±4.39	15.77±5.76	11.22±8.73	12.69±9.66	9.76±2.16	12.43±2.42
	CSW-b	37.02±9.7	0.66±0.09	13.46±2.43	20.11±10.16	16.92±7.49	21.14±6.6	19.91±9.33	23.51±19.74	29.86±18.42	13.85±4.74
	CSW-s	6.33±3.27	0.41±0.18	6.93±2.68	7.11±1.69	14.36±7.01	13.35±7.08	11.82±7.18	7.67±4.64	13.43±8.93	9.01±4.79
	CSW-d	22.36±18.36	0.35±0.06	10.49±2.83	17.85±10.07	12.72±8.06	15.42±6.8	18.25±9.68	12.31±4.21	15.98±8.27	24.82±11.8
2	SW	8.54±7.8	9.24±3.79	0.63±0.16	8.73±3.34	13.28±7.51	11.86±4.23	12.59±6.96	15.69±12.09	9.86±4.11	15.02±12.31
	CSW-b	19.79±6.4	22.5±11.13	0.81±0.29	9.4±3.61	7.64±2.07	15.3±14.47	9.46±8.81	24.4±14.02	13.8±5.79	14.91±8.85
	CSW-s	7.05±4.92	13.19±5.25	0.6±0.16	5.26±3.69	9.01±6.03	18.3±13.13	11.09±10.71	7.52±5.9	9.66±8.72	10.12±13.99
	CSW-d	13.71±8.64	11.59±7.01	0.64±0.3	9.41±8.72	7.19±3.3	11.47±5.3	11.62±8.41	13.51±3.85	8.54±4.0	8.29±6.85
3	SW	10.94±10.43	12.5±3.35	7.71±6.39	0.56±0.09	6.15±4.34	9.42±2.55	8.52±4.97	12.61±8.26	16.88±11.04	5.58±4.21
	CSW-b	21.06±13.03	23.71±18.24	19.08±8.85	0.78±0.16	25.54±9.02	10.23±5.32	12.72±6.25	18.05±10.86	7.33±1.56	16.0±4.06
	CSW-s	18.19±12.12	16.27±14.42	8.06±4.73	0.5±0.31	15.18±11.24	4.76±2.0	8.88±5.27	9.66±6.45	6.99±4.95	8.34±9.14
	CSW-d	10.72±4.99	14.09±7.45	6.73±6.18	0.56±0.17	4.6±1.33	8.03±2.87	12.0±8.28	12.23±5.8	5.16±2.18	10.15±5.44
4	SW	16.21±10.58	12.17±4.06	12.54±10.76	17.58±7.57	0.51±0.1	9.57±3.96	7.79±4.5	12.73±7.48	11.12±3.72	5.6±2.48
	CSW-b	16.27±5.5	25.54±13.63	13.43±3.4	22.14±16.21	0.82±0.12	23.48±23.19	13.3±5.44	13.23±8.83	21.25±15.67	8.53±2.99
	CSW-s	20.57±18.68	14.52±10.89	18.37±13.61	12.49±7.05	0.47±0.25	9.23±9.75	15.37±6.19	7.45±7.09	6.73±6.33	5.59±2.31
	CSW-d	13.65±8.12	15.26±8.16	11.22±7.24	6.18±2.18	0.36±0.05	5.73±3.21	12.19±4.31	9.41±9.01	10.59±3.86	5.98±3.99
5	SW	12.23±5.59	12.99±5.15	17.83±11.12	5.3±2.56	8.37±2.08	0.58±0.08	4.59±3.25	8.8±4.54	5.82±2.61	11.44±3.38
	CSW-b	10.05±4.97	21.11±8.77	19.44±8.42	8.53±3.58	10.85±5.0	0.81±0.28	12.84±6.14	16.5±11.63	13.45±8.48	9.28±4.11
	CSW-s	6.85±4.73	8.2±5.43	10.48±8.54	16.85±18.48	14.13±3.52	0.73±0.2	10.42±4.81	5.49±3.75	3.82±3.15	10.08±5.71
	CSW-d	8.76±4.74	14.61±5.94	11.85±4.81	7.1±3.36	17.0±4.88	0.82±0.39	7.69±4.06	15.36±3.26	11.74±11.53	7.4±5.64
6	SW	16.21±9.44	15.84±6.29	6.59±1.61	7.94±9.3	6.44±2.4	16.24±6.96	0.65±0.16	11.23±2.59	17.33±10.31	7.3±2.58
	CSW-b	21.58±3.87	17.02±5.1	13.73±4.56	19.33±14.03	21.98±11.2	9.84±5.12	1.04±0.52	17.21±8.0	12.87±2.52	9.1±3.99
	CSW-s	18.79±16.51	14.57±8.51	6.2±2.06	14.14±11.12	13.41±9.32	10.95±10.33	0.71±0.09	12.14±9.43	9.59±6.6	6.89±4.66
	CSW-d	19.58±9.77	18.05±9.38	4.7±0.67	14.1±12.84	11.41±2.21	16.39±6.1	0.79±0.24	12.75±4.06	13.21±10.12	12.08±2.4
7	SW	10.44±4.83	11.62±7.83	8.61±5.11	16.65±12.8	9.87±5.8	12.64±2.6	14.57±4.78	0.47±0.14	9.98±3.95	7.49±4.21
	CSW-b	24.07±16.97	26.36±32.13	20.89±16.05	15.88±5.97	11.23±2.97	15.06±9.82	16.84±3.11	0.69±0.11	21.81±9.41	13.48±7.55
	CSW-s	12.37±7.59	12.62±11.39	11.9±12.84	12.97±7.35	16.3±8.65	4.92±2.62	7.9±2.57	0.45±0.2	8.66±7.18	4.69±5.43
	CSW-d	13.13±12.28	12.91±6.65	15.72±7.26	13.89±3.32	7.06±2.4	12.37±4.41	14.19±8.15	0.79±0.34	6.03±2.32	6.07±2.33
8	SW	11.18±3.98	14.19±5.37	6.66±3.28	7.15±4.18	7.82±3.83	5.76±2.75	20.31±12.51	24.66±11.34	0.63±0.12	10.91±6.09
	CSW-b	31.06±18.71	22.14±9.72	10.13±3.45	12.46±8.84	14.29±11.11	9.83±3.62	10.15±4.47	21.86±14.21	0.9±0.18	12.38±5.37
	CSW-s	8.43±6.04	15.39±12.39	4.16±2.58	5.37±2.76	3.35±1.86	4.46±2.26	5.44±4.0	15.2±11.91	0.56±0.19	7.23±3.64
	CSW-d	21.88±12.6	16.54±10.0	13.86±9.91	12.29±11.32	5.14±3.02	5.76±4.77	12.81±13.42	9.39±4.3	0.57±0.16	12.99±8.29
9	SW	18.24±10.84	15.09±4.64	9.86±6.72	9.79±10.32	5.83±5.27	8.39±4.23	9.79±6.82	7.97±4.03	9.41±4.89	0.58±0.11
	CSW-b	16.68±5.5	20.92±7.31	11.42±4.6	22.42±15.27	8.88±2.86	10.05±6.64	13.19±4.39	14.94±9.06	10.37±1.71	0.91±0.23
	CSW-s	7.66±3.52	10.8±8.77	10.83±3.42	8.65±3.32	3.43±2.52	6.33±5.67	8.23±8.12	7.29±3.97	9.77±5.89	0.4±0.16
	CSW-d	13.27±6.99	19.67±10.51	10.97±7.32	15.94±7.08	7.06±4.48	10.1±5.74	15.91±6.66	2.88±1.24	11.62±7.4	0.46±0.1

1. When d is even, $N = \lceil \log_2 d \rceil$, sliced kernels are defined as $K^{(1)} \in \mathbb{R}^{1 \times 2^{-1}d + 1 \times 2^{-1}d + 1}$ and $K^{(h)} \in \mathbb{R}^{1 \times 2^{-h}d + 1 \times 2^{-h}d + 1}$ for $h = 2, \dots, N-1$, and $K^{(N)} \in \mathbb{R}^{1 \times a \times a}$ where $a = \frac{d}{2^{N-1}}$. Then, the non-linear convolution-base slicer $\mathcal{NCS}\text{-}b(X|K^{(1)}, \dots, K^{(N)})$ is defined as:

$$\mathcal{NCS}\text{-}b(X|K^{(1)}, \dots, K^{(N)}) = X^{(N)}, \quad X^{(h)} = \begin{cases} X & h = 0, \\ \sigma(X^{(h-1)} \underset{*}{\overset{1,1}{*}} K^{(h)}) & 1 \leq h \leq N-1, \\ X^{(h-1)} \underset{*}{\overset{1,1}{*}} K^{(h)} & h = N, \end{cases} \quad (13)$$

2. When d is odd, the non-linear convolution-base slicer $\mathcal{NCS}\text{-}b(X|K^{(1)}, \dots, K^{(N)})$ takes the form:

$$\mathcal{NCS}\text{-}b(X|K^{(1)}, \dots, K^{(N)}) = \mathcal{NCS}\text{-}b(\sigma(X \underset{*}{\overset{1,1}{*}} K^{(1)})|K^{(2)}, \dots, K^{(N)}), \quad (14)$$

Table 5: Values of SW and CSW’s variants between probability measures over digits images on MNIST with $L = 10$.

	0	1	2	3	4	5	6	7	8	9	
0	SW	0.57±0.06	20.53±2.52	15.36±2.78	15.74±2.2	18.25±1.54	11.42±3.99	14.46±1.51	15.8±2.52	15.15±1.35	17.48±2.0
	CSW-b	0.71±0.06	31.88±11.67	22.34±3.15	22.98±4.53	20.52±5.56	17.94±2.84	22.32±2.56	26.14±5.25	30.03±6.21	19.28±4.25
	CSW-s	0.58±0.06	20.09±5.51	14.48±7.14	13.06±3.76	16.45±4.3	13.26±2.85	16.7±5.72	20.21±5.67	14.91±4.91	16.94±8.94
	CSW-d	0.52±0.06	21.06±7.2	13.01±2.71	17.36±3.46	16.16±3.39	14.77±3.17	16.7±3.23	21.92±3.09	20.25±8.6	18.55±2.71
1	SW	25.3±7.96	0.43±0.03	16.3±1.96	17.36±2.74	16.39±2.88	14.01±1.93	19.24±3.77	13.23±2.57	15.99±1.78	14.52±2.62
	CSW-b	33.0±6.0	0.65±0.08	20.46±1.46	22.44±1.94	27.12±4.68	23.18±3.97	24.84±2.97	29.08±5.91	25.64±4.54	28.88±5.61
	CSW-s	18.97±9.36	0.46±0.07	18.06±7.38	16.58±4.18	13.58±2.54	12.55±1.78	15.62±6.23	15.54±4.85	13.74±1.98	14.87±3.24
	CSW-d	22.17±2.48	0.43±0.04	16.17±1.43	16.78±4.2	14.93±2.08	12.79±2.63	14.98±3.85	16.9±5.14	13.92±4.58	15.11±3.81
2	SW	14.77±1.8	17.69±1.6	0.64±0.03	10.28±1.96	12.22±2.12	11.73±2.48	11.5±3.53	13.53±1.72	9.6±1.85	13.15±2.57
	CSW-b	21.49±4.99	23.43±6.43	0.83±0.05	18.58±3.28	18.32±2.29	18.96±2.85	16.8±3.66	18.31±2.3	16.2±2.87	18.84±5.18
	CSW-s	16.89±4.26	17.57±2.08	0.63±0.07	11.13±3.82	13.88±5.17	12.61±5.01	11.15±1.74	14.28±2.33	10.19±2.03	16.62±4.35
	CSW-d	21.28±4.15	17.16±3.04	0.63±0.06	12.09±3.81	14.79±1.78	12.25±4.75	11.71±2.14	17.2±1.54	12.32±2.76	15.63±2.79
3	SW	15.66±4.87	16.82±2.5	14.42±1.92	0.6±0.07	13.62±1.41	8.05±0.6	15.11±2.59	12.19±1.27	10.52±2.78	14.35±3.08
	CSW-b	24.73±8.19	23.51±3.83	16.3±3.95	0.76±0.12	25.57±3.7	10.64±0.96	22.13±5.06	24.77±6.63	16.83±1.66	21.49±5.49
	CSW-s	15.61±5.91	15.03±5.75	9.41±3.99	0.55±0.07	12.78±4.56	8.72±3.2	11.83±2.8	14.65±4.16	7.58±3.0	13.59±1.91
	CSW-d	15.88±2.67	14.94±3.43	10.75±1.56	0.65±0.06	14.7±3.18	8.24±1.22	13.83±5.09	13.33±3.79	10.0±1.62	14.11±2.86
4	SW	18.5±1.38	16.94±2.19	12.31±3.21	13.48±2.23	0.55±0.05	10.39±1.66	13.25±2.24	9.44±2.86	11.15±2.01	6.83±1.49
	CSW-b	25.1±5.55	25.62±6.12	18.14±3.41	24.22±4.88	0.84±0.07	18.9±1.36	14.25±2.79	18.08±6.55	18.37±1.48	12.07±2.52
	CSW-s	19.48±7.65	15.57±5.95	13.02±4.05	15.87±1.25	0.55±0.13	11.82±1.29	13.8±3.54	10.48±2.78	13.51±2.76	6.73±1.7
	CSW-d	16.17±1.16	18.11±5.31	13.21±3.01	15.01±1.24	0.55±0.08	13.47±3.11	11.53±1.48	8.78±2.06	12.27±1.25	7.32±2.04
5	SW	11.35±2.37	14.34±2.0	11.84±1.76	8.13±1.63	10.46±0.77	0.62±0.07	8.42±0.95	12.71±2.66	7.38±0.95	10.03±1.81
	CSW-b	17.33±7.32	23.97±3.93	18.03±3.14	11.4±2.14	17.3±1.86	0.81±0.03	13.77±2.15	16.37±2.63	13.99±1.74	18.16±3.73
	CSW-s	13.45±4.62	13.66±2.71	11.13±2.89	8.25±1.46	12.8±3.12	0.59±0.08	12.31±2.51	13.14±2.75	5.94±2.38	10.63±3.61
	CSW-d	11.79±1.47	14.45±4.43	10.99±3.76	8.79±2.58	12.68±4.04	0.67±0.08	11.24±2.05	12.57±1.41	8.5±2.28	11.65±2.85
6	SW	15.6±1.2	16.65±3.04	10.63±1.99	15.93±3.09	12.5±1.05	12.58±3.18	0.66±0.07	15.37±3.21	11.68±2.11	12.12±3.93
	CSW-b	21.15±4.67	26.98±3.01	14.98±1.48	22.54±4.87	18.32±3.14	17.24±4.15	1.04±0.1	23.68±6.73	15.94±1.41	17.94±3.6
	CSW-s	18.83±4.56	16.09±4.05	13.72±3.78	15.24±4.06	13.0±4.2	17.12±4.06	0.64±0.08	17.28±4.99	11.69±3.35	11.74±2.59
	CSW-d	16.12±3.72	14.69±3.83	11.43±1.67	10.75±1.92	13.95±3.16	15.15±1.79	0.69±0.15	17.14±1.65	12.42±2.7	13.24±4.31
7	SW	18.55±2.71	14.24±2.65	14.61±1.6	14.12±2.33	11.79±2.89	12.15±2.79	17.08±1.51	0.72±0.09	12.67±2.78	7.98±1.63
	CSW-b	24.17±4.74	25.38±6.42	21.83±8.2	22.54±3.56	19.95±5.58	16.28±2.96	21.13±2.93	0.9±0.14	19.6±2.63	12.73±3.11
	CSW-s	12.47±1.5	15.36±0.97	15.23±3.91	12.71±1.72	10.69±3.32	12.01±5.21	17.81±5.83	0.61±0.06	13.33±6.67	9.56±2.85
	CSW-d	19.4±4.62	17.74±3.06	15.3±3.29	10.51±2.69	12.01±2.19	11.87±2.01	15.7±3.37	0.7±0.1	12.91±1.35	9.49±2.61
8	SW	14.99±1.95	13.63±2.87	9.59±2.8	8.77±1.09	11.89±2.73	7.5±1.87	12.93±2.57	13.43±0.92	0.59±0.07	11.0±1.95
	CSW-b	24.82±3.3	20.56±1.82	15.07±2.03	15.51±1.18	18.82±3.58	11.73±0.52	16.3±3.85	19.28±2.76	0.93±0.16	13.9±3.14
	CSW-s	15.49±4.93	13.59±3.22	12.38±2.73	9.3±0.57	13.71±2.37	7.81±3.45	17.73±7.39	12.52±4.11	0.67±0.09	11.11±2.33
	CSW-d	15.19±4.72	13.92±2.28	11.3±2.84	10.36±2.18	13.92±3.61	8.26±1.93	11.13±2.68	13.94±1.75	0.61±0.07	10.63±2.94
9	SW	18.69±3.5	15.59±2.36	13.37±0.4	12.71±2.73	7.36±1.82	10.05±2.31	13.42±2.92	8.5±2.18	11.33±1.33	0.61±0.07
	CSW-b	25.66±7.64	24.44±1.89	20.66±6.8	22.19±6.0	9.87±1.96	15.43±1.32	16.71±4.28	15.41±2.76	15.67±2.73	0.8±0.12
	CSW-s	15.6±3.63	19.29±5.63	10.75±3.21	14.83±3.5	8.66±2.2	10.49±2.57	13.57±2.71	7.91±2.74	11.98±3.98	0.61±0.08
	CSW-d	18.11±2.98	15.13±3.83	14.29±2.38	13.52±3.24	7.41±1.78	10.48±0.75	11.89±1.63	11.17±3.27	11.17±2.6	0.54±0.08

where $K^{(1)} \in \mathbb{R}^{d \times d}$ and $K^{(2)}, \dots, K^{(N)}$ are the corresponding sliced kernels that are defined on the dimension $d - 1$.

The main idea of non-linear convolution-based slicer is that we incorporate non-linear activation function $\sigma(\cdot)$ into the layers of the convolution-base slicer. Using that idea, we also can extend the convolution-stride and convolution-dilation slicers to their nonlinear versions, named non-linear convolution-stride and convolution-dilation slicers. We respectively denote these slicers as $\mathcal{NCS-s}(X|K^{(1)}, \dots, K^{(N)})$ and $\mathcal{NCS-d}(X|K^{(1)}, \dots, K^{(N)})$.

Using the non-linear convolution-base slicer for sliced Wasserstein, we obtain the corresponding non-linear convolution-base sliced Wasserstein as follows.

Definition 8. For any $p \geq 1$, the non-linear convolution-base sliced Wasserstein ($\mathcal{NCSW-b}$) of order



Figure 8: Random generated images of CSW-b and CSW-d on CIFAR10.

$p > 0$ between two given probability measures $\mu, \nu \in \mathcal{P}_p(\mathbb{R}^{c \times d \times d})$ is given by:

$$\mathcal{NCSW}\text{-}b_p(\mu, \nu) :=$$

$$\left(\mathbb{E}_{K^{(1)} \sim \mathcal{U}(\mathcal{K}^{(1)}), \dots, K^{(N)} \sim \mathcal{U}(\mathcal{K}^{(N)})} \left[W_p^p \left(\mathcal{NCS}\text{-}b(\cdot | K^{(1)}, \dots, K^{(N)}) \# \mu, \mathcal{NCS}\text{-}b(\cdot | K^{(1)}, \dots, K^{(N)}) \# \nu \right) \right] \right)^{\frac{1}{p}}, \quad (15)$$

where $\mathcal{NCS}\text{-}b(\cdot | K^{(1)}, \dots, K^{(N)})$ is a non-linear convolution-base slicer with $K^{(i)} \in \mathbb{R}^{c^{(i)} \times k^{(i)} \times k^{(i)}}$ for any $i \in [N]$ and $\mathcal{U}(\mathcal{K}^{(i)})$ is the uniform distribution with the realizations being in the set $\mathcal{K}^{(i)} = \left\{ K^{(i)} \in \mathbb{R}^{c^{(i)} \times k^{(i)} \times k^{(i)}} \mid \sum_{h=1}^{c^{(i)}} \sum_{i'=1}^{k^{(i)}} \sum_{j'=1}^{k^{(i)}} K_{h,i',j'}^{(i)2} = 1 \right\}$.

By replacing the non-linear convolution-base slicer $\mathcal{NCS}\text{-}b(\cdot | K^{(1)}, \dots, K^{(N)})$ in Definition 15 by non-linear convolution-stride slicer $\mathcal{NCS}\text{-}s(\cdot | K^{(1)}, \dots, K^{(N)})$ and non-linear convolution-dilation slicer $\mathcal{NCS}\text{-}d(\cdot | K^{(1)}, \dots, K^{(N)})$, we respectively have the non-linear convolution-stride sliced Wasserstein (NCSW-s) and non-linear convolution-dilation sliced Wasserstein (NCSW-d). In Appendix C, we provide experiment results with non-linear convolution sliced Wasserstein on generative models.



Figure 9: Random generated images of CSW-b and CSW-d on CelebA.

C Additional Experiments

Comparing Measures over MNIST’s digits: Similar to the result in the main text with $L = 100$, we present the values of SW and CSW’s variants between probability measures over digits-images with $L = 1$ and $L = 10$ in Table 4 and Table 5. We observe that with a smaller value of L , the standard deviations of 5 different runs of both SW and CSW’s variants are higher than values with $L = 100$.

Random generated images of CSW-b and CSW-d: We show some images that are drawn randomly from models trained by CSW and CSW-d on CIFAR10, CelebA, STL10, and CelebA-HQ in Figure 8, Figure 9, Figure 10, and Figure 11 in turn. From these figures, we again observe the effect of changing the number of projections L , namely, a bigger value of L leads to better generated images. Also, the qualitative comparison between CSW-b and CSW-d is consistent with the quantitative comparison via FID scores and IS scores in Table 2.

Results of non-linear convolution sliced Wasserstein: We report FID scores and IS scores of generative models trained by non-linear sliced Wasserstein (NSW) [23] and non-linear convolution sliced Wasserstein (NCSW) variants including NCSW-b, NCSW-s, and NCSW-d on CIFAR10 in Table 6. The non-linear sliced Wasserstein is a variant of generalized sliced Wasserstein where we use a non-linear activation function after the linear projection, namely, $g(x, \theta) = \sigma(\theta^\top x)$. For NSW and NCSW variants, we choose $\sigma(\cdot)$ as the Sigmoid function. Compared to linear versions in Table 2,

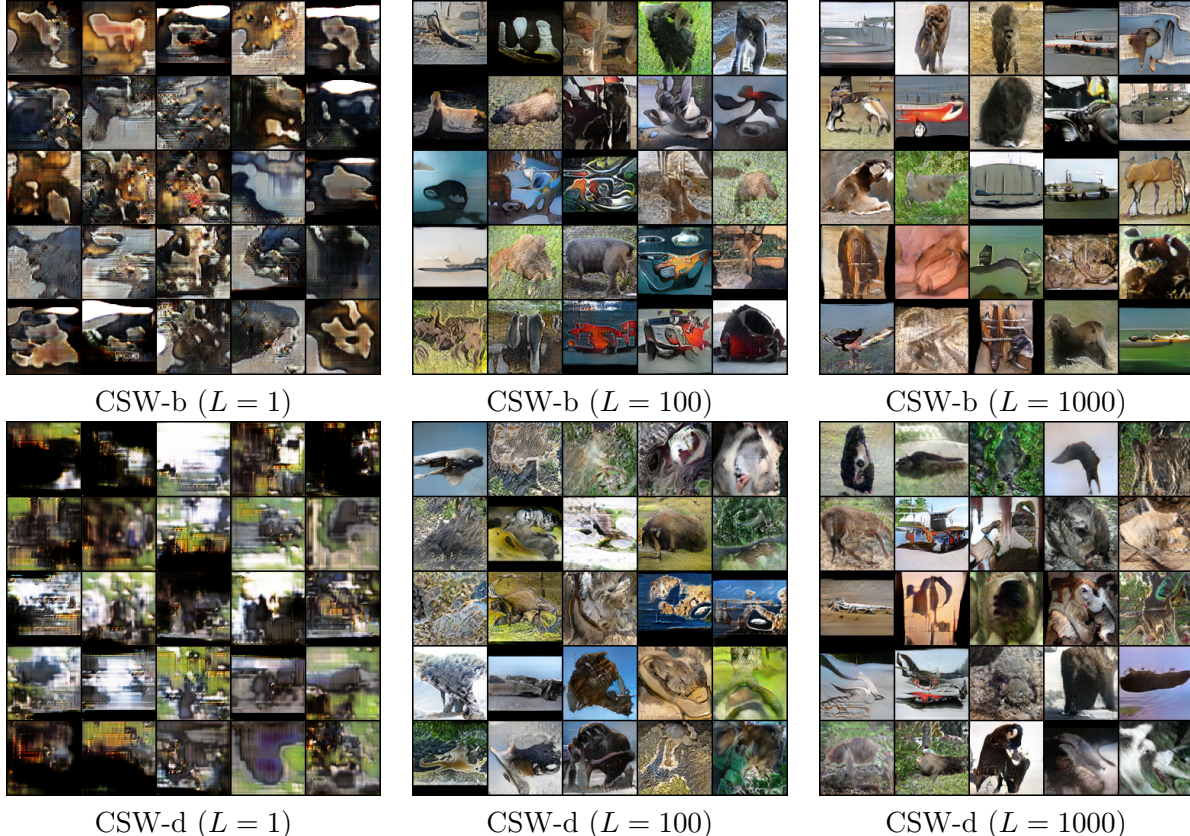


Figure 10: Random generated images of CSW-b and CSW-d on STL10.

we can see that including the non-linear activation function can improve the scores in some cases, e.g., NSW and NCSW-s. We also show FID scores and IS scores across training epochs in Figure 12. Similar to the linear case, NCSW’s variants can help generative models converge faster than NSW.

D Experimental Settings

Architectures of neural network: We illustrate the detail of neural network architectures including the generative networks and the discriminative networks on CIFAR10 in Table 7, CelebA in Table 8, STL10 in Table 9, and CelebA-HQ in Table 10.

Other settings: We set the number of training iterations to 50000 on CIFAR10, CelebA, and CelebA-HQ and to 100000 on STL10. For each 5 iterations, we update the generator G_ϕ by the corresponding SW and CSW variants. For the discriminator, we update T_{β_1} and T_{β_2} every iterations. We set the mini-batch size m to 128 on CIFAR10 and CelebA, set to 32 on STL10, and set to 16 on CelebA-HQ. The learning rate of G_ϕ , T_{β_1} , and T_{β_2} is set to 0.0002. We use Adam [22] for optimization problems with $(\beta_1, \beta_2) = (0, 0.9)$.

Calculation of scores: For the FID scores and the Inception scores, we calculate them based on 50000 random samples from trained models. For the FID scores, we calculate the statistics of datasets on all training samples.

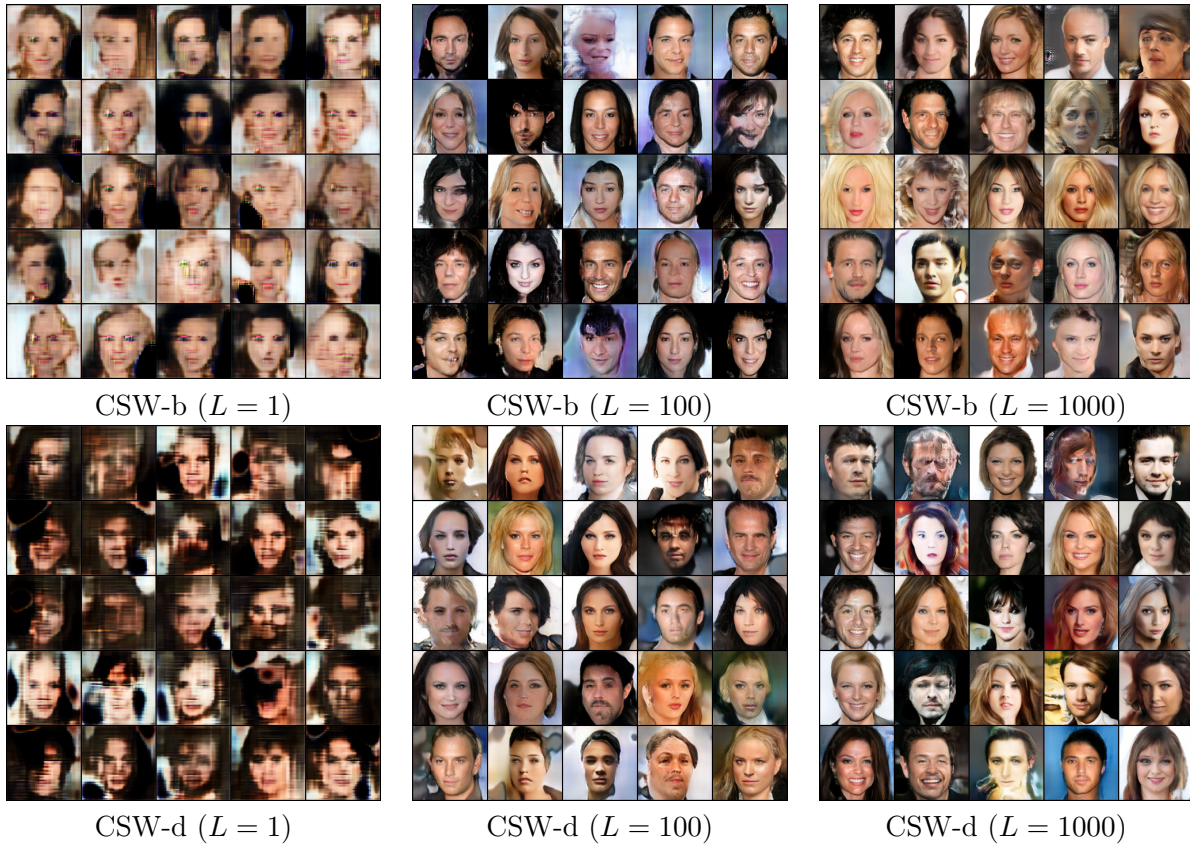


Figure 11: Random generated images of CSW-b and CSW-d on CelebA-HQ.

Table 6: Summary of FID and IS scores of NSW and NCSW variants on CIFAR10 (32x32).

Method	CIFAR10 (32x32)	
	FID (\downarrow)	IS (\uparrow)
NSW (L=1)	83.58	3.76
NCSW-b (L=1)	82.19	3.74
NCSW-s (L=1)	79.09	4.42
NCSW-d (L=1)	75.94	3.92
NSW (L=100)	52.99	5.33
NCSW-b (L=100)	50.25	5.60
NCSW-s (L=100)	44.56	5.91
NCSW-d (L=100)	45.91	6.04
NSW (L=1000)	43.73	6.03
NCSW-b (L=1000)	44.03	5.98
NCSW-s (L=1000)	30.21	6.97
NCSW-d (L=1000)	42.30	6.31

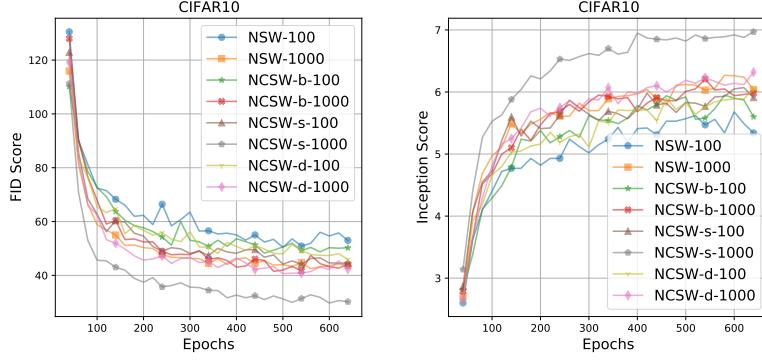


Figure 12: FID scores and IS scores over epochs of different training non-linear losses on CIFAR10. We observe that NCSW variants usually help the generative models converge faster.

Table 7: CIFAR10 architectures.

(a) G_ϕ	(b) T_{β_1}	(c) T_{β_2}
Input: $\epsilon \in \mathbb{R}^{128} \sim \mathcal{N}(0, 1)$	Input: $\mathbf{x} \in [-1, 1]^{32 \times 32 \times 3}$	Input: $\mathbf{x} \in \mathbb{R}^{128 \times 8 \times 8}$
128 \rightarrow 4 \times 4 \times 256, dense linear	ResBlock down 128	ReLU
ResBlock up 256	ResBlock down 128	Global sum pooling
ResBlock up 256	ResBlock down 128	128 \rightarrow 1
ResBlock up 256	ResBlock 128	Spectral normalization
BN, ReLU, 3 \times 3 conv, 3 Tanh	ResBlock 128	

Table 8: CelebA architectures.

(a) G_ϕ	(b) T_{β_1}	(c) T_{β_2}
Input: $\epsilon \in \mathbb{R}^{128} \sim \mathcal{N}(0, 1)$	Input: $\mathbf{x} \in [-1, 1]^{64 \times 64 \times 3}$	Input: $\mathbf{x} \in \mathbb{R}^{128 \times 8 \times 8}$
128 \rightarrow 4 \times 4 \times 256, dense linear	ResBlock down 128	ReLU
ResBlock up 256	ResBlock down 128	Global sum pooling
ResBlock up 256	ResBlock down 128	128 \rightarrow 1
ResBlock up 256	ResBlock 128	Spectral normalization
ResBlock up 256	ResBlock 128	
ResBlock up 256	ResBlock 128	
BN, ReLU, 3 \times 3 conv, 3 Tanh	ResBlock 128	

Table 9: STL10 architectures.

(a) G_ϕ	(b) T_{β_1}	(c) T_{β_2}
Input: $\epsilon \in \mathbb{R}^{128} \sim \mathcal{N}(0, 1)$	Input: $\mathbf{x} \in [-1, 1]^{96 \times 96 \times 3}$	Input: $\mathbf{x} \in \mathbb{R}^{128 \times 6 \times 6}$
128 \rightarrow 3 \times 3 \times 256, dense , linear	ResBlock down 128	ReLU
ResBlock up 256	ResBlock down 128	Global sum pooling
ResBlock up 256	ResBlock down 128	128 \rightarrow 1
ResBlock up 256	ResBlock down 128	Spectral normalization
ResBlock up 256	ResBlock 128	
ResBlock up 256	ResBlock 128	
ResBlock up 256	ResBlock 128	
BN, ReLU, 3 \times 3 conv, 3 Tanh		

Table 10: CelebA-HQ architectures.

(a) G_ϕ	(b) T_{β_1}	(b) T_{β_2}
Input: $\epsilon \in \mathbb{R}^{128} \sim \mathcal{N}(0, 1)$	Input: $\mathbf{x} \in [-1, 1]^{128 \times 128 \times 3}$	Input: $\mathbf{x} \in \mathbb{R}^{128 \times 8 \times 8}$
128 \rightarrow 4 \times 4 \times 256, dense , linear	ResBlock down 128	ReLU
ResBlock up 256	ResBlock down 128	Global sum pooling
ResBlock up 256	ResBlock down 128	128 \rightarrow 1
ResBlock up 256	ResBlock down 128	Spectral normalization
ResBlock up 256	ResBlock 128	
ResBlock up 256	ResBlock 128	
ResBlock up 256	ResBlock 128	
BN, ReLU, 3 \times 3 conv, 3 Tanh		

References

- [1] J. Altschuler, J. Niles-Weed, and P. Rigollet. Near-linear time approximation algorithms for optimal transport via Sinkhorn iteration. In *Advances in Neural Information Processing Systems*, pages 1964–1974, 2017. (Cited on page 1.)
- [2] M. Arjovsky, S. Chintala, and L. Bottou. Wasserstein generative adversarial networks. In *International Conference on Machine Learning*, pages 214–223, 2017. (Cited on page 1.)
- [3] B. Bhushan Damodaran, B. Kellenberger, R. Flamary, D. Tuia, and N. Courty. Deepjdot: Deep joint distribution optimal transport for unsupervised domain adaptation. In *Proceedings of the European Conference on Computer Vision (ECCV)*, pages 447–463, 2018. (Cited on page 1.)
- [4] S. Bobkov and M. Ledoux. ‘One-dimensional empirical measures, order statistics, and Kantorovich transport distances. *Memoirs of the American Mathematical Society*, 261, 2019. (Cited on page 10.)
- [5] C. Bonet, N. Courty, F. Septier, and L. Drumetz. Sliced-Wasserstein gradient flows. *arXiv preprint arXiv:2110.10972*, 2021. (Cited on page 10.)
- [6] N. Bonneel, J. Rabin, G. Peyré, and H. Pfister. Sliced and Radon Wasserstein barycenters of measures. *Journal of Mathematical Imaging and Vision*, 1(51):22–45, 2015. (Cited on pages 2 and 3.)
- [7] X. Chen, Y. Yang, and Y. Li. Augmented sliced Wasserstein distances. *International Conference on Learning Representations*, 2022. (Cited on page 10.)
- [8] A. Coates, A. Ng, and H. Lee. An analysis of single-layer networks in unsupervised feature learning. In *Proceedings of the fourteenth international Conference on Artificial Intelligence and Statistics*, pages 215–223. JMLR Workshop and Conference Proceedings, 2011. (Cited on pages 11 and 12.)
- [9] N. Courty, R. Flamary, A. Habrard, and A. Rakotomamonjy. Joint distribution optimal transportation for domain adaptation. In *Advances in Neural Information Processing Systems*, pages 3730–3739, 2017. (Cited on page 1.)
- [10] M. Cuturi. Sinkhorn distances: Lightspeed computation of optimal transport. In *Advances in Neural Information Processing Systems*, pages 2292–2300, 2013. (Cited on page 1.)
- [11] B. Dai and U. Seljak. Sliced iterative normalizing flows. In *International Conference on Machine Learning*, pages 2352–2364. PMLR, 2021. (Cited on page 10.)
- [12] I. Deshpande, Y.-T. Hu, R. Sun, A. Pyrros, N. Siddiqui, S. Koyejo, Z. Zhao, D. Forsyth, and A. G. Schwing. Max-sliced Wasserstein distance and its use for GANs. In *Proceedings of the IEEE Conference on Computer Vision and Pattern Recognition*, pages 10648–10656, 2019. (Cited on page 2.)
- [13] I. Deshpande, Z. Zhang, and A. G. Schwing. Generative modeling using the sliced Wasserstein distance. In *Proceedings of the IEEE Conference on Computer Vision and Pattern Recognition*, pages 3483–3491, 2018. (Cited on pages 2 and 11.)

- [14] N. Fournier and A. Guillin. On the rate of convergence in Wasserstein distance of the empirical measure. *Probability Theory and Related Fields*, 162:707–738, 2015. (Cited on pages 1 and 10.)
- [15] K. Fukushima and S. Miyake. Neocognitron: A self-organizing neural network model for a mechanism of visual pattern recognition. In *Competition and cooperation in neural nets*, pages 267–285. Springer, 1982. (Cited on pages 2 and 4.)
- [16] Z. Goldfeld and K. Greenewald. Sliced mutual information: A scalable measure of statistical dependence. *Advances in Neural Information Processing Systems*, 34, 2021. (Cited on page 10.)
- [17] I. Goodfellow, Y. Bengio, and A. Courville. *Deep learning*. MIT press, 2016. (Cited on page 2.)
- [18] K. He, X. Zhang, S. Ren, and J. Sun. Deep residual learning for image recognition. In *Proceedings of the IEEE Conference on Computer Vision and Pattern Recognition*, pages 770–778, 2016. (Cited on pages 2 and 11.)
- [19] M. Heusel, H. Ramsauer, T. Unterthiner, B. Nessler, and S. Hochreiter. GANs trained by a two time-scale update rule converge to a local Nash equilibrium. In *Advances in Neural Information Processing Systems*, pages 6626–6637, 2017. (Cited on page 12.)
- [20] N. Ho, X. Nguyen, M. Yurochkin, H. H. Bui, V. Huynh, and D. Phung. Multilevel clustering via Wasserstein means. In *International Conference on Machine Learning*, pages 1501–1509, 2017. (Cited on page 1.)
- [21] M. Huang, S. Ma, and L. Lai. A Riemannian block coordinate descent method for computing the projection robust Wasserstein distance. In *International Conference on Machine Learning*, pages 4446–4455. PMLR, 2021. (Cited on page 10.)
- [22] D. P. Kingma and J. Ba. Adam: A method for stochastic optimization. *arXiv preprint arXiv:1412.6980*, 2014. (Cited on page 26.)
- [23] S. Kolouri, K. Nadjahi, U. Simsekli, R. Badeau, and G. Rohde. Generalized sliced Wasserstein distances. In *Advances in Neural Information Processing Systems*, pages 261–272, 2019. (Cited on pages 2, 8, and 25.)
- [24] S. Kolouri, P. E. Pope, C. E. Martin, and G. K. Rohde. Sliced Wasserstein auto-encoders. In *International Conference on Learning Representations*, 2018. (Cited on page 2.)
- [25] S. Kolouri, G. K. Rohde, and H. Hoffmann. Sliced Wasserstein distance for learning Gaussian mixture models. In *Proceedings of the IEEE Conference on Computer Vision and Pattern Recognition*, pages 3427–3436, 2018. (Cited on page 2.)
- [26] A. Krizhevsky, G. Hinton, et al. Learning multiple layers of features from tiny images. *Master’s thesis, Department of Computer Science, University of Toronto*, 2009. (Cited on pages 11 and 12.)
- [27] A. Krizhevsky, I. Sutskever, and G. E. Hinton. Imagenet classification with deep convolutional neural networks. *Advances in Neural Information Processing Systems*, 25, 2012. (Cited on page 2.)
- [28] T. Le, T. Nguyen, N. Ho, H. Bui, and D. Phung. Lamda: Label matching deep domain adaptation. In *International Conference on Machine Learning*, pages 6043–6054. PMLR, 2021. (Cited on page 1.)

- [29] Y. LeCun, L. Bottou, Y. Bengio, and P. Haffner. Gradient-based learning applied to document recognition. *Proceedings of the IEEE*, 86(11):2278–2324, 1998. (Cited on page 11.)
- [30] C.-Y. Lee, T. Batra, M. H. Baig, and D. Ulbricht. Sliced Wasserstein discrepancy for unsupervised domain adaptation. In *Proceedings of the IEEE/CVF Conference on Computer Vision and Pattern Recognition*, pages 10285–10295, 2019. (Cited on page 2.)
- [31] J. Lezama, W. Chen, and Q. Qiu. Run-sort-rerun: Escaping batch size limitations in sliced Wasserstein generative models. In *International Conference on Machine Learning*, pages 6275–6285. PMLR, 2021. (Cited on page 10.)
- [32] T. Lin, C. Fan, N. Ho, M. Cuturi, and M. Jordan. Projection robust Wasserstein distance and Riemannian optimization. *Advances in Neural Information Processing Systems*, 33:9383–9397, 2020. (Cited on page 10.)
- [33] T. Lin, N. Ho, X. Chen, M. Cuturi, and M. I. Jordan. Fixed-support Wasserstein barycenters: Computational hardness and fast algorithm. In *NeurIPS*, pages 5368–5380, 2020. (Cited on page 1.)
- [34] T. Lin, N. Ho, and M. Jordan. On efficient optimal transport: An analysis of greedy and accelerated mirror descent algorithms. In *International Conference on Machine Learning*, pages 3982–3991, 2019. (Cited on page 1.)
- [35] T. Lin, N. Ho, and M. I. Jordan. On the efficiency of the Sinkhorn and Greenkhorn algorithms and their acceleration for optimal transport. *ArXiv Preprint: 1906.01437*, 2019. (Cited on page 1.)
- [36] Z. Liu, P. Luo, X. Wang, and X. Tang. Deep learning face attributes in the wild. In *Proceedings of International Conference on Computer Vision (ICCV)*, December 2015. (Cited on pages 11 and 12.)
- [37] A. Liutkus, U. Simsekli, S. Majewski, A. Durmus, and F.-R. Stöter. Sliced-Wasserstein flows: Nonparametric generative modeling via optimal transport and diffusions. In *International Conference on Machine Learning*, pages 4104–4113. PMLR, 2019. (Cited on page 10.)
- [38] G. Mena and J. Weed. Statistical bounds for entropic optimal transport: sample complexity and the central limit theorem. In *Advances in Neural Information Processing Systems*, 2019. (Cited on page 2.)
- [39] N. Naderializadeh, J. Comer, R. Andrews, H. Hoffmann, and S. Kolouri. Pooling by sliced-Wasserstein embedding. *Advances in Neural Information Processing Systems*, 34, 2021. (Cited on page 10.)
- [40] K. Nadjahi, V. De Bortoli, A. Durmus, R. Badeau, and U. Şimşekli. Approximate Bayesian computation with the sliced-Wasserstein distance. In *ICASSP 2020-2020 IEEE International Conference on Acoustics, Speech and Signal Processing (ICASSP)*, pages 5470–5474. IEEE, 2020. (Cited on page 10.)
- [41] K. Nadjahi, A. Durmus, P. E. Jacob, R. Badeau, and U. Simsekli. Fast approximation of the sliced-Wasserstein distance using concentration of random projections. *Advances in Neural Information Processing Systems*, 34, 2021. (Cited on page 10.)

- [42] K. Nadjahi, A. Durmus, U. Simsekli, and R. Badeau. Asymptotic guarantees for learning generative models with the sliced-Wasserstein distance. In *Advances in Neural Information Processing Systems*, pages 250–260, 2019. (Cited on page 10.)
- [43] F.-P. Paty and M. Cuturi. Subspace robust Wasserstein distances. In *International Conference on Machine Learning*, pages 5072–5081, 2019. (Cited on page 10.)
- [44] O. Pele and M. Werman. Fast and robust earth mover’s distances. In *2009 IEEE 12th International Conference on Computer Vision*, pages 460–467. IEEE, September 2009. (Cited on page 1.)
- [45] G. Peyré and M. Cuturi. Computational optimal transport: With applications to data science. *Foundations and Trends® in Machine Learning*, 11(5-6):355–607, 2019. (Cited on page 3.)
- [46] G. Peyré and M. Cuturi. Computational optimal transport, 2020. (Cited on page 1.)
- [47] J. Radon. 1.1 über die bestimmung von funktionen durch ihre integralwerte längs gewisser mannigfaltigkeiten. *Classic papers in modern diagnostic radiology*, 5:21, 2005. (Cited on page 8.)
- [48] A. Rakotomamonjy and R. Liva. Differentially private sliced Wasserstein distance. In *International Conference on Machine Learning*, pages 8810–8820. PMLR, 2021. (Cited on page 10.)
- [49] M. Rowland, J. Hron, Y. Tang, K. Choromanski, T. Sarlos, and A. Weller. Orthogonal estimation of Wasserstein distances. In *The 22nd International Conference on Artificial Intelligence and Statistics*, pages 186–195. PMLR, 2019. (Cited on page 10.)
- [50] T. Salimans, I. Goodfellow, W. Zaremba, V. Cheung, A. Radford, and X. Chen. Improved techniques for training GANs. *Advances in Neural Information Processing Systems*, 29, 2016. (Cited on page 12.)
- [51] V. Titouan, R. Flamary, N. Courty, R. Tavenard, and L. Chapel. Sliced Gromov-Wasserstein. *Advances in Neural Information Processing Systems*, 32, 2019. (Cited on page 10.)
- [52] I. Tolstikhin, O. Bousquet, S. Gelly, and B. Schoelkopf. Wasserstein auto-encoders. In *International Conference on Learning Representations*, 2018. (Cited on page 1.)
- [53] C. Villani. *Optimal transport: Old and New*. Springer, 2008. (Cited on pages 1 and 3.)
- [54] M. J. Wainwright. *High-dimensional statistics: A non-asymptotic viewpoint*. Cambridge University Press, 2019. (Cited on page 19.)
- [55] J. Wu, Z. Huang, D. Acharya, W. Li, J. Thoma, D. P. Paudel, and L. V. Gool. Sliced Wasserstein generative models. In *Proceedings of the IEEE Conference on Computer Vision and Pattern Recognition*, pages 3713–3722, 2019. (Cited on page 2.)
- [56] J. Xu, H. Zhou, C. Gan, Z. Zheng, and L. Li. Vocabulary learning via optimal transport for neural machine translation. In *Proceedings of the 59th Annual Meeting of the Association for Computational Linguistics and the 11th International Joint Conference on Natural Language Processing (Volume 1: Long Papers)*, pages 7361–7373, 2021. (Cited on page 1.)

- [57] K. D. Yang, K. Damodaran, S. Venkatachalapathy, A. C. Soylemezoglu, G. Shivashankar, and C. Uhler. Predicting cell lineages using autoencoders and optimal transport. *PLoS computational biology*, 16(4):e1007828, 2020. (Cited on page 1.)
- [58] M. Yi and S. Liu. Sliced Wasserstein variational inference. In *Fourth Symposium on Advances in Approximate Bayesian Inference*, 2021. (Cited on page 10.)